ANALYZING HYDRAULIC FRACTURES USING TIME-LAPSE ELECTRIC POTENTIAL DATA

A THESIS
SUBMITTED TO THE DEPARTMENT OF ENERGY RESOURCES ENGINEERING
AND THE COMMITTEE ON GRADUATE STUDIES
OF STANFORD UNIVERSITY
IN PARTIAL FULFILLMENT OF THE REQUIREMENTS
FOR THE DEGREE OF
MASTER OF SCIENCE

Jason Hu
June 2018

© Copyright by Jason Hu 2018
All Rights Reserved

I certify that I have read this thesis and that, in my opinion, it is fully adequate in scope and quality as a dissertation for the degree of Master of Science in Engineering Resources Engineering.

(Roland Horne) Principal Adviser

Abstract

Hydraulic fracturing is the process of injecting fluids at high pressure to create conductive channels in low permeability reservoirs so that oil and gas can flow through. Hydraulic fracturing will continue to play a key role in the future of oil and gas production, and characterizing the fractures is an important task to improve the understanding and utilization of the process. As an approach to augment and improve on the existing methods, resistivity measurements can be used to characterize subsurface features. The lithology, pore fluid chemistry, and water content affect the spatial distribution of resistive and capacitive characteristics of the subsurface (Magnusdottir and Horne, 2015). Fractures created by hydraulic fracturing are saturated with water and show reduced resistivity, which provides the opportunity to extract fracture characteristics by monitoring the change in resistivity distribution in the subsurface as a function of time.

The purpose of this work was to investigate a fracture characterization approach by making use of electrical potential data. We focused mainly on using electric field simulation and inverse analysis to examine subsurface electric field behavior due to fracture creation. We considered a new borehole method designed specifically for hydraulic fracture characterization, which modifies a single-borehole survey method and utilizes a permanent resistivity array. This method can attain higher resolution by implementing electrodes in or near boreholes and monitoring the electric potential distribution near the horizontal fracture zone.

The electric potential distribution in steady-state flow through a porous medium is analogous to the electrical potential distribution in an electrically conductive medium. By solving the flow equation and the Poisson equation for electrical field numerically,

we can determine the fluid distribution and electric potential distribution at every time interval (Dey A. and Morrison H.F., 1977). The time-lapse electrical data generated by the simulator was considered as measured data and subsequently used for analyzing fracture characteristics. Inverse analysis was used in this work to find fracture parameters such as fracture length, orientation, and more. By deploying our simulator as the forward model, we used an objective function to capture the difference between measured data and data generated by the forward guess. Then we used a gradient-free nonlinear optimization scheme to minimize the objection function in order to achieve the best guess of targeted parameters.

The preliminary results of this work show that time-lapse electrical data is capable of capturing flow dynamics during fracturing process and has the potential to further assist fracture characterization.

Acknowledgments

First and foremost, I would like to express my sincere gratitude to Professor Roland Horne for his advice and guidance throughout my two years at Stanford University. Professor Horne's passion and dedication for science have inspired me to stay focused on science and technology.

I am really grateful to Dr. Pavel Tomin for his advice and support on the subject of numerical simulation. Dr. Tomin was always willing to answer my questions, and helped me tackle many challenges ever since I came to Stanford. I also want to thank Dr. Timur Garipov and Dr. Mohammad Karimi-Fard for their help and suggestions regarding flow simulation and fracture modeling. I am thankful for all the members of SUPRI-D research group. The discussions and recommendations provided by everyone in the group have made a great difference in my work.

I am grateful for many friends and colleagues I met here at Stanford, especially EJ Baik, Greg Von Wald, Dante Orta, and Srinikaeth Thiru. Their company have made the past two years one of the most enjoyable time of my life, and I will forever cherish our friendship no matter where I am.

I am indebted to my parents Chunyun Tang and Xiaolin Hu for the unconditional support they have provided me. I would not be who I am today without their love and understanding. I also want to thank my girlfriend Jane Sima for always being there for me. Her professionalism and work ethic have motivated me to work hard every single day of my life.

Finally, I want to thank SUPRI-D for the generous financial support of this research.

Contents

Abstract **iv**

Acknowledgments **vi**

1 Introduction **1**

1.1 Background and Motivation 1

1.2 Electrical Resistivity Tomography 2

1.3 Objectives 3

2 Reservoir Model **5**

2.1 AD-GPRS 5

2.2 Fracture Modeling 6

2.3 Permanent Resistivity Array Design 7

2.3.1 Case Study 1 - Ketzin, Germany 8

2.3.2 Case Study 2 - Cranfield, MS, U.S 9

2.3.3 Horizontal Well Resistivity Array Design 10

3 Electric Potential Modeling **12**

3.1 Governing Equations 12

3.2 Finite Volume Method 15

3.3 Analytical Solution 15

3.4 Numerical Model Compared to Analytical Model 18

4 Parameter Estimation **23**
4.1 Procedures for Parameter Estimation 23
4.2 Objective Function 25
4.3 Optimization of Objective Function 25
4.3.1 Generalized Pattern Search 26
4.3.2 Nelder-Mead Simplex Algorithm 30

5 Implementation **33**
5.1 Unstructured Grid Model 35
5.2 Structured Grid Model 36

6 Sensitivity Analysis **40**
6.1 Location Sensitivity 40
6.2 Injection Fluid Electrical Conductivity Sensitivity 41
6.3 Noise Sensitivity 43

7 Results and Findings **53**
7.1 Parameter Estimation Without Noise 53
7.1.1 Fracture Length Estimate 54
7.1.2 Fracture Length And Fracture Density Estimate 57
7.2 Parameter Estimation With Noise 58
7.2.1 Fracture Length Estimate 58
7.2.2 Fracture Length And Fracture Density Estimate 58
7.2.3 Estimate Uncertainty 63

8 Concluding Remarks **68**
8.1 Conclusion 68
8.2 Future Work 69

List of Tables

3.1 Units. 13

5.1 Reservoir Model Parameters 34
5.2 Fracture Parameters 34
5.3 Electric Model Parameters 35

6.1 Resistivity of common materials 43

List of Figures

1.1 Cross-borehole electrical resistivity tomography (Magnusdottir, 2013) 3
1.2 Single-borehole electrical resistivity tomography (Binley and Kemna, 2005) 4

2.1 Structured and unstructured implementation of reservoir grid. 8
2.2 Ketzin field array design and VERA schematics (Schmidt-Hattenberger et al., 2011) 9
2.3 Cranfield project array design (Carrigan et al., 2013) 10
2.4 Resistivity array setup 11

3.1 Two-dimensional discretization 16
3.2 Two source electrodes and their respective images 18
3.3 Analytical solution of electric potential in two-dimensional rectangular domain 19
3.4 Numerical solution in two-dimensional rectangular domain 20
3.5 Numerical error in two-dimensional 20
3.6 Numerical method vs. analytical method 21

4.1 Work flow for parameter estimation 24
4.2 Examples of positive spanning set D 27
4.3 Two steps of Generalized Pattern Search 29
4.4 Five operations of Nelder-Mead Simplex Method 32

5.1 Two-dimensional horizontal flow reservoir model 34
5.2 Unstructured implementation 36

5.3 Pressure recordings at measurement points 1 and 2 for 20 simulations using different mesh sizes 37
5.4 Electric potential recordings between measurement points 1 and 2 for 20 simulations using different mesh sizes 38
5.5 Objective function evaluations of 20 simulations using different mesh sizes 38
5.6 Structured Implementation 39

6.1 Electrode location sensitivity 42
6.2 Injection fluid conductivity sensitivity 44
6.3 Example of typical time-lapse potential measurement (Schmidt-Hattenberger et al., 2011). Signal qualities: regular (a,b), asymptotic discharging with spikes (c), random(d). 45
6.4 Generalized Pattern Search performance on noisy data(one parameter search) 46
6.5 Nelder-Mead Simplex method performance on noisy data(one parameter search) 47
6.6 Generalized Pattern Search performance on noisy data(two parameter search) 49
6.7 Generalized Pattern Search performance on noisy data(two parameter search) 50
6.8 Nelder-Mead Simplex method performance on noisy data(two parameter search) 51
6.9 Nelder-Mead Simplex method performance on noisy data(two parameter search) 52

7.1 Reservoir with $45m$ fractures and fracture density 0.005 fractures/m^3 54
7.2 Fracture length estimate by applying Generalized Pattern Search on perfectly measured data. 55
7.3 Fracture length estimate by applying Nelder-Mead on perfectly measured data. 56

7.4 Fracture length and fracture density estimate by applying Generalized Pattern Search on perfectly measured data. 59
7.5 Fracture length and fracture density estimate by applying Nelder-Mead on perfectly measured data. 60
7.6 Fracture length estimate by applying Generalized Pattern Search on noisy data with signal to ratio of 50. 61
7.7 Fracture length estimate by applying Nelder-Mead on noisy data with signal to ratio of 50. 62
7.8 Fracture length and fracture density estimate by applying Generalized Pattern Search on noisy data with signal to ratio of 50. 64
7.9 30 noise realizations 65
7.10 Uncertainty of fracture length estimate at signal to noise ratio 50 . . 66
7.11 Uncertainty of fracture density estimate at signal to noise ratio 50 . . 67

Chapter 1

Introduction

1.1 Background and Motivation

Hydraulic fracturing has become one of the mostly frequently used operations to tackle unconventional reservoirs. Through hydraulic fracturing, oil producers can create flow channels inside of low permeability zones for oil and gas to flow through. There is no doubt hydraulic fracturing will keep playing a key role in the future of oil and gas exploration and production. To improve the understanding of the hydraulic fracturing process, many efforts have been put into fracture characterization. Fracture length and fracture density are two important attributes of fracture characterization; some of the notable methods used to investigate these two attributes include the P3D model, well testing, microseismic, and tiltmeters:

- P3D model is a mathematical model that calculates fracture area based on fracture fluid leak-off characteristics of the rock formation, and it is an extension to the two-dimensional (PKN) model by adding height variation. The downside of the P3D model is that fracture length is inferred, not measured. In addition, the P3D model is highly dependent on the assumptions in the model, and estimates vary greatly depending on the assumptions (Adachi and Peirce, 2010).

- Well testing uses pressure buildup tests following fracture treatment to estimate fracture length. There are two uncertainties with well testing methods: first,

large uncertainties depending on the assumptions. Second, lack of prefracture well test data (Bennett et al., 2005).

- The microseismic method uses downhole measurements of time-dependent induced microseismicity to interpret fracture length. However, these measurements are difficult to interpret and optimally require nearby offset wells (Bennett et al., 2005)

- Tiltmeter measures fracture-induced deformation in a nearby offset well, and inverts the data to interpret fracture characteristics (Wright et al., 1998). The tiltmeter method can be difficult to interpret and it is expensive to conduct in the field.

1.2 Electrical Resistivity Tomography

Resistivity measurements can be used to characterize subsurface features because lithology, pore fluid chemistry, and water content affect the spatial distribution of low-frequency resistive and capacitive characteristics of soil. Resistivity data have been proven to be successful in characterizing oil and gas reservoirs and geothermal reservoirs. Most rock formation materials are electrical insulators where the internal electric charges are not allowed to move freely. Formation fluids are usually electrical conductors with hydrocarbons being the exception, because hydrocarbons are theoretically infinitely resistive. Therefore, a rock formation that is porous and saturated with salty water has lower overall electrical resistivity than nonporous formation or formation contains hydrocarbons. Building on this principle, resistivity surveys can be an important tool in evaluating subsurface formations. Resistivity surveys work by injecting a steady-state electrical current into the ground and observing the resulting distribution of potentials at the surface or within boreholes. Data from electric resistivity surveys contains information about how charges are distributed at boundaries where electrical conductivity changes, thus creating opportunities for us to learn more about subsurface features. Resistivity survey data can be interpreted to infer rock formation porosity, saturation, and permeability.

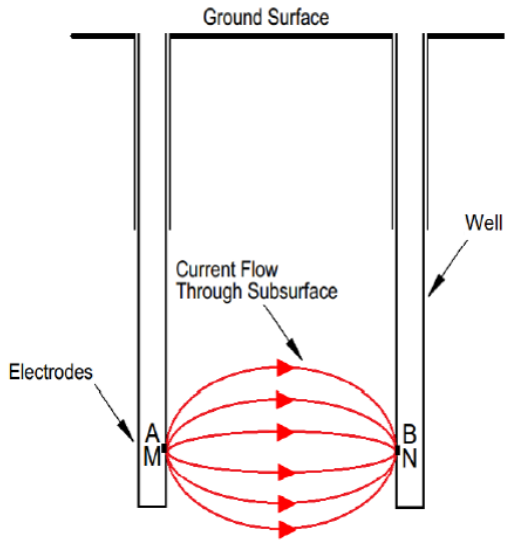

Figure 1.1: Cross-borehole electrical resistivity tomography (Magnusdottir, 2013)

Electrical resistivity surveys were made practical by the Schlumberger brothers in the 1920s, and the applications expanded from surface surveys to subsurface surveys. Among electrical resistivity survey methods, borehole surveys are of most relevant interest to us. Cross-borehole surveys and single-borehole surveys have been used in geothermal and mineral exploration applications, and the physics of these surveys are similar to oil and gas exploration principles. Fig. 1.1 illustrates an example of cross-borehole survey, and Fig. 1.2 illustrates an example of single-borehole survey.

1.3 Objectives

Hydraulic fractures are created by injecting water into the wellbore at extremely high pressure. Under high pressure, the rock formation is fractured, thus creating conductive pathways for water to get into the rock matrix and reduce the resistivity of the matrix. Due to the resistivity change in the rock matrix, there are opportunities to extract fracture characteristics by continuously monitoring the change in resistivity distribution in the rock matrix. The objective of this research was to examine the feasibility of using time-lapse electrical resistivity data to characterize hydraulic

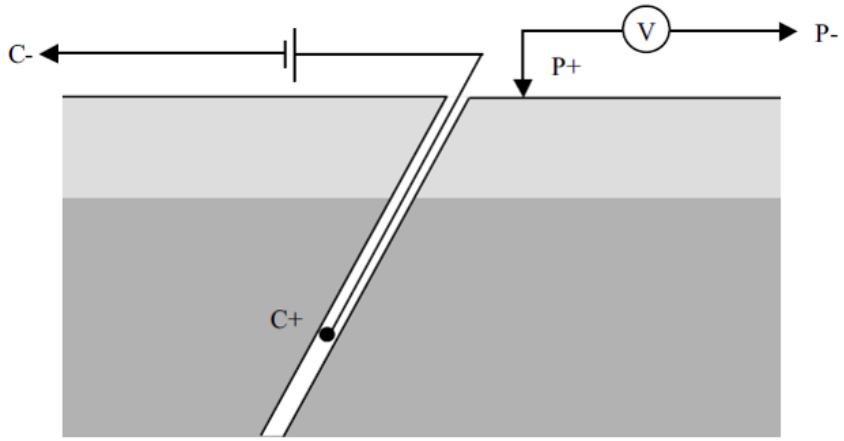

Figure 1.2: Single-borehole electrical resistivity tomography (Binley and Kemna, 2005)

fractures created in unconventional oil and gas operations. We first investigated the impact hydraulic fractures have on electrical resistivity of rock formations. Then we combined fluid simulation and electric potential simulation to obtain time-lapse electric potential signals that capture the dynamic flow system and inverted the signal. After setting up the framework of parameter searching, we analyzed and inverted the electric potential signal to estimate the fracture length and fracture density of the fractured formation. Last, we tested the sensitivity of our algorithm in various scenarios with different values of parameters.

Chapter 2

Reservoir Model

In this chapter we will introduce the reservoir model used to conduct our study as well as the electrical resistivity array setup for monitoring electric potentials in time-lapse. We will introduce Automatic-Differentiation General Purpose Research Simulator (AD-GPRS) (Rin et al., 2017), a flow simulator used to assist physics modeling for the purpose of this study. Hydraulic fracture modeling is central to this study, and we will discuss how to appropriately model these fractures by using discrete feature modeling. Lastly, we will introduce a new design of permanent downhole resistivity array. We will explain how the array is set up and how it can be incorporated into the reservoir model we constructed to investigate fracture properties.

2.1 AD-GPRS

The reservoir model used for this study was constructed and simulated using Automatic-Differentiation General Purpose Research Simulator (AD-GPRS). AD-GPRS is developed and maintained by the SUPRI-B group at Stanford Energy Resources Engineering department. AD-GPRS is a state-of-the-art reservoir simulator with distinct features such as fractured reservoir simulation and multiphysics simulation. AD-GPRS solves the governing partial differential equations by first discretizing the domain of interest with the finite volume method, and subsequently approximating the solution using the Newton-Ralphson method. AD-GPRS was chosen as the reservoir simulator

for this research because it uses a built-in automatic differentiation framework which allows flexible treatment of nonlinear physics formulation. Such treatment of the nonlinear physics formulations makes it possible to conduct electric potential simulation in parallel with flow simulation because the equation that describes electric potential is analogous to the equation that describes pressure. This ability to solve both flow equation and electric potential equation enables us to construct a multiphysics forward simulation that fully encapsulates saturation distribution information into the electric potential signals, and is critical to inversion of time-lapse electric potential data.

2.2 Fracture Modeling

The random distribution and multiscale features are two distinctive features that make hydraulic fractures extremely difficult to model. In addition, the geomechanical characteristics of creating hydraulic fractures are complex, which increases the difficulty of constructing an accurate mathematical model and the corresponding numerical simulation to describe fluid flow in fractured media. One of the methods developed to better capture some of the random characteristics of fractured media is Discrete Feature Modeling (DFM).

Discrete features are surfaces defining discontinuities in rock properties. Examples of discrete features include formation features that are created artificially such as hydraulic fractures, or formation features that occur naturally, such as fractured rock, faults and compaction bands. These discrete features are difficult to model because they require more geological data and need more powerful computational capabilities. Karimi-Fard and Firoozabadi first adopted DFM to solve multiphase flow in fractured media in 2001 (Karimi-Fard and Firoozabadi, 2001). Hydraulic fractures in the DFM are present explicitly in the discretized grid, thus reducing the dimensions needed for computation. There are two main advantages of DFM:

1. Fractures are treated as separate entities in the discretized domain. Relationships between fractures and unfractured reservoir can be established without the

necessity to use interporosity flow functions. This explicit fracture treatment effectively reduces computational cost without sacrificing solution accuracy.

2. Fractures in DFM have assigned porosity and permeability. Both matrix permeability and fracture permeability are considered in the model and this helps not only define the fluid flow within the fractures, but also define the fluid flow between fractures and the neighboring porous media. This consistent treatment of all components of the reservoir domain captures the heterogeneous character of fractured media and allows appropriate solution of fluid flow in such scenarios.

In this study we modeled hydraulic fractures using DFM, and explored the implementation of the discrete feature model in an unstructured grid design as shown in Fig. 2.1(a) and structured grid design as shown in Fig. 2.1(b). The motivation to use unstructured grid representation was to keep the arbitrary characteristics of the development and distribution for hydraulic fractures, and capture the heterogeneity, discontinuity, and anisotropy properties of hydraulic fractures. It is worth noting that DFM was not applicable at the reservoir scale, so all the fractured reservoir domain used for simulation in this study were rectangular cuboids with boundaries less than 100 meters. We constructed the model as an unconventional reservoir with low permeability and high initial oil saturation. For the reservoir excluding fractures, we specified porosity to be 0.2, permeability to be 1 millidarcy, and initial water saturation to be 0.2. For the hydraulic fractures, we specified porosity to be 100%, permeability to be 1000 millidarcy, and fracture aperture to be 0.001 meter. We also made assumptions that all hydraulic fractures in the model have the same length and same orientation.

2.3 Permanent Resistivity Array Design

There has been progress in the development of deep permanent downhole resistivity arrays in recent years. In this section we will first take a look at two pilot projects - one in Ketzin, Germany, and one in Cranfield, Mississippi, where permanent resistivity arrays have been used to monitor the migration of CO_2 plumes. We will show the

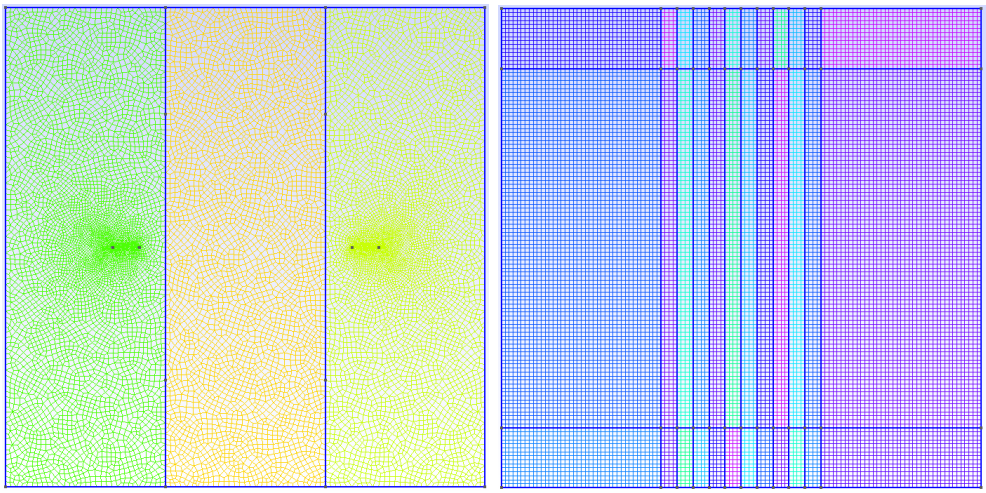

(a) Unstructured implementation (b) Structured implementation

Figure 2.1: Structured and unstructured implementation of reservoir grid.

practical aspect of resistivity array implementation, and how that can be translated into our own implementation of monitoring hydraulic fractures.

2.3.1 Case Study 1 - Ketzin, Germany

The permanent resistivity array system for CO_2 migration detection at the Ketzin pilot site in Germany was the deepest application of permanent geoelectric monitoring system in Europe (Schmidt-Hattenberger et al., 2011). Ketzin is located 40 km west of Berlin and is home to the longest running on-shore CO_2 storage site. The project was initiated in 2004, and over 67,000 tonnes of CO_2 were injected into the reservoir between 2008 and 2013. The target formation of the storage reservoir is the Triassic Stuttgart formation, a saline sandstone formation at a depth of about 630m to 640m below the surface. A set of permanent electrode arrays was installed deep downhole behind casing at three wells (one injection well and two monitoring wells) at the Ketzin site to track CO_2 related signals for the life-cycle of the injection project. Three Vertical Electrical Resistivity Arrays (VERA) that consist a total of 45 stainless-steel electrodes were placed behind stainless steel metallic casing covered with insulating textile materials (Schmidt-Hattenberger et al., 2011). The site wells

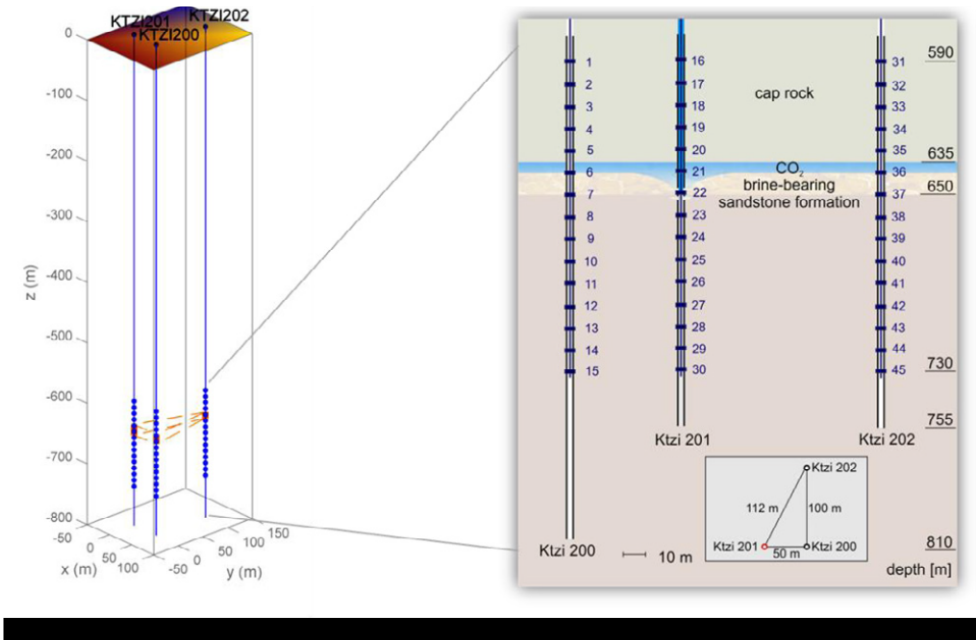

Figure 2.2: Ketzin field array design and VERA schematics (Schmidt-Hattenberger et al., 2011)

design and electrodes placements can be visualized in Fig. 2.2.

2.3.2 Case Study 2 - Cranfield, MS, U.S

The Cranfield site is located 16 miles east of Natchez, Mississippi where it used to be a productive oil and gas field from the 1940s to the 1960s. The target reservoir for CO_2 storage is a 20-28m thick fluvial Lower Tuscaloosa Sandstone located at a depth of 3000m below the surface. Over one million tons of CO_2 have been injected into this deep saline formation since the beginning of the project. There are three wells in total: one injection well and two monitoring wells. The three wells are in a colinear arrangement with monitoring well F2 70 m away from injection well F1 and monitoring well F3 33 m away from monitoring well F2. The layout of the site design is shown in Fig.2.3. A cross-well electrical resistivity tomography (ERT) system was installed and operated successfully for more than a year for this project, and it is the deepest application of ERT to date (Carrigan et al., 2013). A vertical array composed of 14 different electrodes with 4.6 m spacing and 61 m total length was

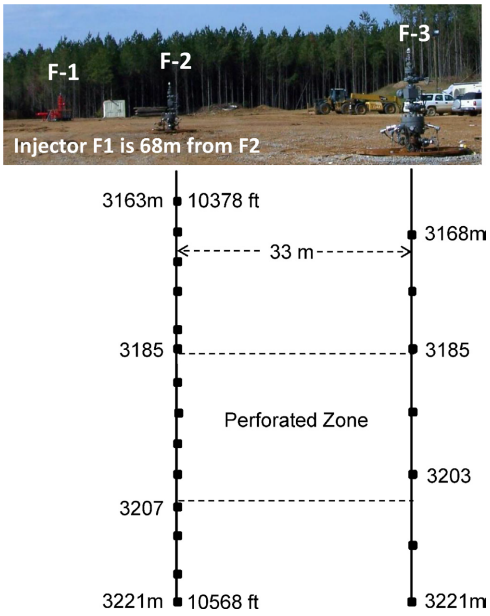

Figure 2.3: Cranfield project array design (Carrigan et al., 2013)

installed on monitoring well F2. The system uses stainless steel electrodes mounted on a fiberglass casing with epoxy-based centralizers. The cables connected to the electrodes are encapsulated by steel casing and they run upward along the casing to a custom designed splitter that provide transition from each individual electrode cable to combined seven-conductor cables (Carrigan et al., 2013).

2.3.3 Horizontal Well Resistivity Array Design

In this study we explored a novel technique of conducting electrical resistivity surveys for unconventional oil and gas operations. By combining a cross-borehole survey method with a single-borehole survey method, we established a new borehole method designed specifically for monitoring electric potential at different locations along the wellbore in deep reservoir formations. A simplified schematic of the proposed electrical resistivity array is shown in Fig. 2.4. This resistivity array is composed of two current electrodes (one source electrode and one sink electrode) and two potential measuring electrodes. Compared to the resistivity arrays used in the projects

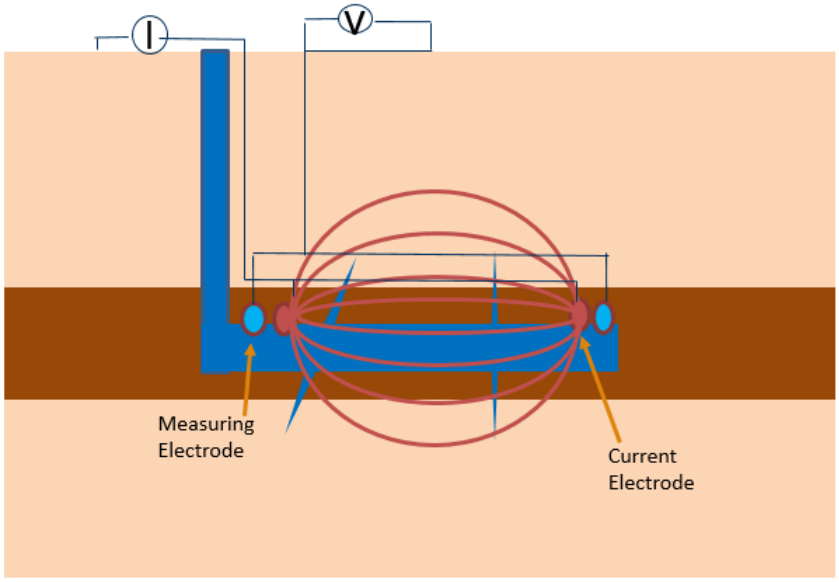

Figure 2.4: Resistivity array setup

described previously, this tool has significantly fewer electrodes in the array, thus reducing the complexity and the cost for monitoring. This array would be installed in boreholes outside of casing and monitor the potential distribution near the fracture zone. The advantage of having the resistivity array near the borehole is twofold:

1. The current flow between the source electrode and the sink electrode is localized to the fractured zone, which in turn will provide stronger signals if there are any changes in the subsurface electric conductivities.

2. The potential measuring electrodes can be placed as close to the fractured media as possible. This can help reduce the effect of other environment factors on electric potential signals as well as help acquire higher data resolution.

Chapter 3

Electric Potential Modeling

Electrical potential modeling was an integral part of the study not only to generate electric signals that respond to the dynamic reservoir environment, but also to construct the appropriate forward model for parameter estimation. In this chapter we will talk about the governing equations and fundamentals of electric potential field modeling. We will discuss our approach of solving the governing mass balance equation in details, and we will show the accuracy of the numerical model by comparing it to an analytical model.

3.1 Governing Equations

The main requirement of electric potential modeling is to solve the Poisson equation describing the electric potential field. Dey and Morrison described how to derive the Poisson Equation from the basic electrical relationships between voltage, current density, electrical conductivity and electric field (Dey A. and Morrison H.F., 1977). To derive the Poisson equation for electric potential field, we first start from Ohm's law, which relates current density, $\boldsymbol{J}$, electrical conductivity of the medium, σ, and the electric field, $\boldsymbol{E}$, as:

$$\boldsymbol{J} = \sigma \boldsymbol{E}. \tag{3.1}$$

Table 3.1: Units.

Quantity	Symbol	Units
Current density	$\boldsymbol{J}$	$\mathrm{A/m^2}$
Electric field	$\boldsymbol{E}$	V/m
Electric potential	V	V
Conductivity	σ	$\mathrm{mhos{\cdot}m^{-1}}$
Current density	q	$\mathrm{A/m^3}$

The electric field is equal to the negative gradient of the electric potential, V, i.e.:

$$\boldsymbol{E} = -\nabla V. \tag{3.2}$$

Then substituting the electric field in Eq. 3.1 with the derived electric field expression in Eq. 3.2, we have:

$$\boldsymbol{J} = -\left(\sigma \nabla V\right) \tag{3.3}$$

Finally, apply the principle of conservation of a point charge in a control volume, and utilizing the fact that the divergence of electric current density is the same as current, we can obtain the Poisson equation that describes the electric potential field:

$$\nabla^2 \cdot V = -\frac{q(x,y)}{\sigma}. \tag{3.4}$$

We see in the derived expression shown in Eq. 3.4 that electric potential at a certain point in the medium can be obtained as long as we have the electric conductivity of the medium, the strength of the electric current source, and the location of the electrical current source.

For a medium consisting of solid and fluid phases, we have two options to evaluate the effective electrical conductivity: Archie's Law, and the volume-averaged method.

- Archie's law (Archie, 1942) is arguably one of the most important development in petrophysics and laid the foundation for modern well logging interpretation. Archie's law relates electrical resistivity of the conductive medium to the brine saturation of the medium, and thus allows one to infer hydrocarbon saturations

indirectly. Archie's Law can be described as Eq. 3.5:

$$\sigma^{-1} = d\phi^{-e}\sigma_w^{-1}, \tag{3.5}$$

where $d = 1.0$ and $e = 2.0$ are empirical constants. For the dependence of σ_w^{-1} on temperature, T, we have (Ucok et al., 1980):

$$\sigma_w^{-1} = b_0 + b_1 T^{-1} + b_2 T + b_3 T^2 + b_4 T^3, \tag{3.6}$$

and for dependence on concentration, c:

$$\sigma_w^{-1} = \frac{10}{\Lambda c}, \tag{3.7}$$

where $\Lambda = B_0 - B_1\sqrt{c} + B_2 c \ln c$. Archie's Law is the most widely used equation relating formation resistivity to fluid saturation, but it is not without limitations. Archie's Law make strong assumptions about pore geometries as well as formation properties, and does not apply when there are more than one conductive fluid existing in the formation (Glover, 2010). For this study we are interested not only in the correct solution describing electric potential, but also in the electric properties of reservoir formation components and how they affect parameter estimation. Thus we avoided using Archie's Law due to these limitations.

- The Volume-averaged equation is a general expression relating electric conductivity of all formation components, saturations of fluids in the formation, and porosity of the rock formation. The equation is described as Eq. 3.8.

$$\sigma = \phi\sigma_r + (1 - \phi)\sum_p S_p\sigma_p, \tag{3.8}$$

where ϕ is the porosity, S_p is the saturation of a fluid phase, and σ_α is the conductivity of a phase. The volume-averaged method takes account of the electric properties of rock and fluids. The change of fluid saturation, fluid

properties can all be reflected appropriately in the electrical conductivity of the porous medium and thus is our chosen approach.

3.2 Finite Volume Method

In this study we used the Finite Volume Method to approximate the solution to Eq. 3.4 using a point discretization of the subsurface, a method for electric potential problem introduced by Dey and Morrison(Dey A. and Morrison H.F., 1977). For a two-dimensional rectangular reservoir, the subsurface is discretized into $N_x \times N_y$ blocks using this method, and the Poisson equation for electrical potential is:

$$\frac{\partial}{\partial x}[\sigma(\frac{\partial V}{\partial x})] + \frac{\partial}{\partial y}[\sigma(\frac{\partial V}{\partial y})] + q(x,y) = 0 \tag{3.9}$$

Eq. 3.9 can be integrated over a control volume as described by the green region in Fig. 3.1. After integration we obtain:

$$\int_{\Delta V} \frac{\partial}{\partial x}(\sigma\frac{\partial V}{\partial x})dx.dy + \int_{\Delta V} \frac{\partial}{\partial y}(\sigma\frac{\partial V}{\partial y})dx.dy + \int_{\Delta V} q(x,y)dx.dy = 0 \tag{3.10}$$

Applying the divergence theorem and using finite difference approximation, the above equation can be written as:

$$\begin{aligned}(\sigma_x)_{i-\frac{1}{2},j}[V_{i-1,j} - V_{i,j}]\frac{\Delta y\Delta z}{\Delta x} + (\sigma_x)_{i+\frac{1}{2},j}[V_{i+1,j} - V_{i,j}]\frac{\Delta y\Delta z}{\Delta x} \\ +(\sigma_y)_{i,j-\frac{1}{2}}[V_{i,j-1} - V_{i,j}]\frac{\Delta x\Delta z}{\Delta y} + (\sigma_y)_{i,j+\frac{1}{2}}[V_{i,j+1} - V_{i,j}]\frac{\Delta x\Delta z}{\Delta y} \\ +I\delta(x_i - x_s)\delta(y_i - y_s)\delta(z_i - z_s) = 0\end{aligned} \tag{3.11}$$

3.3 Analytical Solution

We solved the Poisson equation for electric potential in a two-dimensional homogeneous medium in order to verify the numerical solution introduced in this chapter.

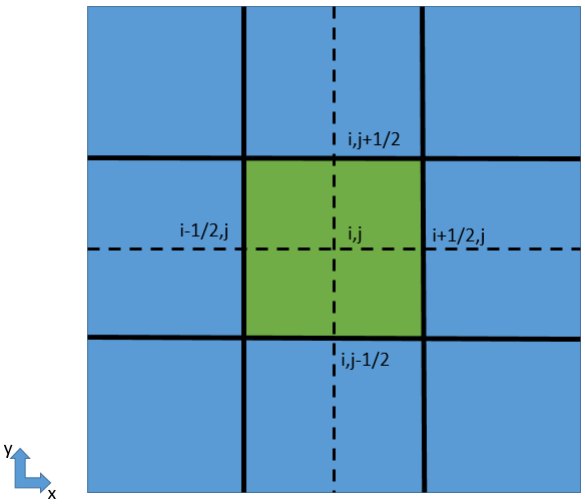

Figure 3.1: Two-dimensional discretization

Because the volume of a current source or sink electrode is negligible compared to the volume of the reservoir, we can consider each current source or sink electrode as a point source. Then we can proceed to solve the Poisson equation for electric potential of a rectangular domain using Green's functions (Greennberg, 1971). The Green's functions have the general form:

$$\nabla^2 \cdot G(X; X_0) = \delta(X - X_0). \tag{3.12}$$

where $\delta(X - X_0)$ is Dirac Delta function that describes a point source. X represents the coordinates of the location we wish to evaluate, and X_0 represents the coordinates of the source or sink location. The Dirac Delta function has the following characteristics:

$$\int_{-\infty}^{\infty} \delta(X) = 1.0 \tag{3.13}$$

and $\delta(X) = 0$ if $X \neq 0$, ∞ if $X = 0$.

We use the Dirac Delta function δ to represent point source or sink, (x,y) to represent the location of a given point in this two-dimensional domain, and voltage V can be represented by Green's function G. Let $q(x, y) = \mu\delta(x, y)$, where μ represent

the magnitude of charge, then

$$\nabla^2 V = -\frac{\mu\delta(x,y)}{\sigma}. \tag{3.14}$$

applying the Divergence Theorem in a two-dimensional circle with radius R,

$$\iint_{r\leq R} \nabla\cdot(\nabla V) d_{volume} = \iint_{r\leq R} -\frac{\mu\delta(x,y)}{\sigma} d_{volume}. \tag{3.15}$$

becomes

$$\oint_{r=R} \nabla\cdot V\cdot \boldsymbol{n} d_l = -\frac{\mu}{\sigma}. \tag{3.16}$$

$$V(x,y) = -\frac{\mu}{2\pi\sigma}\ln\left(\sqrt{(x-x_0)^2+(y-y_0)^2}\right) + constant. \tag{3.17}$$

where (x_0, y_0) is the location of the source. Now we arrive at the analytical solution for electric potential caused by a point source excitation in two-dimensional geometry with infinite far boundaries.

Reservoir simulators generally use no-flow boundaries, or Neumann boundaries for the boundary conditions of the problem. Poisson equation was solved numerically using Neumann boundary conditions in order to be consistent with the flow solution, so here we also solved the Green's function for electric potential also with Neumann boundary conditions. To find the Neumann solution of electric potential in a two-dimensional rectangular domain, we used the Principle of Superposition. The Principle of Superposition is a powerful tool in reservoir engineering used to cope with complex situations using only simple models. By laying out the same sources or sinks in space and summing all of them up, one can use superposition to create solutions for constant radial flow, dual porosity, fractured and bounded well (Horne, 1995). To construct analytical solution to Green's function in a two-dimensional rectangular domain with no flow boundaries, we set mirror images of the current source electrode and current sink electrode with respect to boundaries of the reservoir as shown in Fig. 3.2. The black square box in the figure is the reservoir domain; the blue dot inside of the reservoir domain is the current sink electrode, and the red dot inside

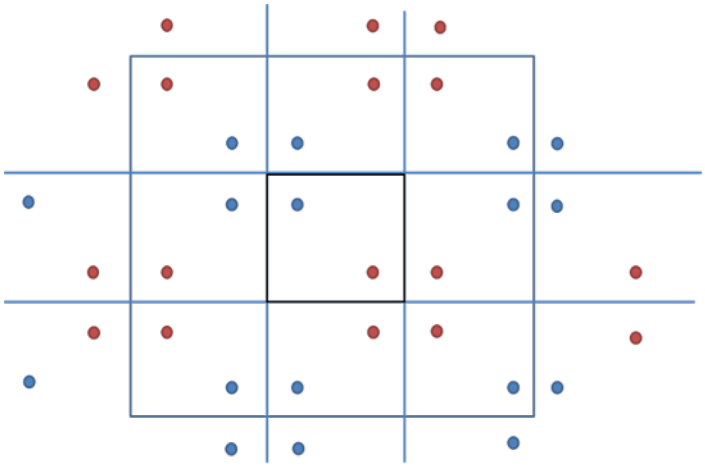

Figure 3.2: Two source electrodes and their respective images

of the reservoir domain is the current source electrode. All the dots outside square reservoir domain are images of the source and sink electrode, and this mirroring pattern of electrodes extends to infinity. To find the electric voltage of a location in the domain, we superposed solutions of both current source and sink electrodes as well as all the mirror images at this specific location. This can be expressed as:

$$\begin{aligned} V(x,y) = &\sum_{i=0}^{\infty} -\frac{\mu_{source}}{2\pi\sigma} \ln\left(\sqrt{(x-x_i)^2+(y-y_i)^2}\right) \\ &+\sum_{j=0}^{\infty} -\frac{\mu_{sink}}{2\pi\sigma} \ln\left(\sqrt{(x-x_j)^2+(y-y_j)^2}\right) \\ &+constant. \end{aligned} \tag{3.18}$$

where i is for source electrodes, and j is for sink electrodes.

3.4 Numerical Model Compared to Analytical Model

To compare the numerical model and analytical model we simulated the electric potential field for a two-dimensional rectangular shaped reservoir with dimension $100m \times 100m$. The source electrode was placed at (10m,90m) with electric current rate specified at 1 ampere, and the sink electrode was placed at (90m,10m) with

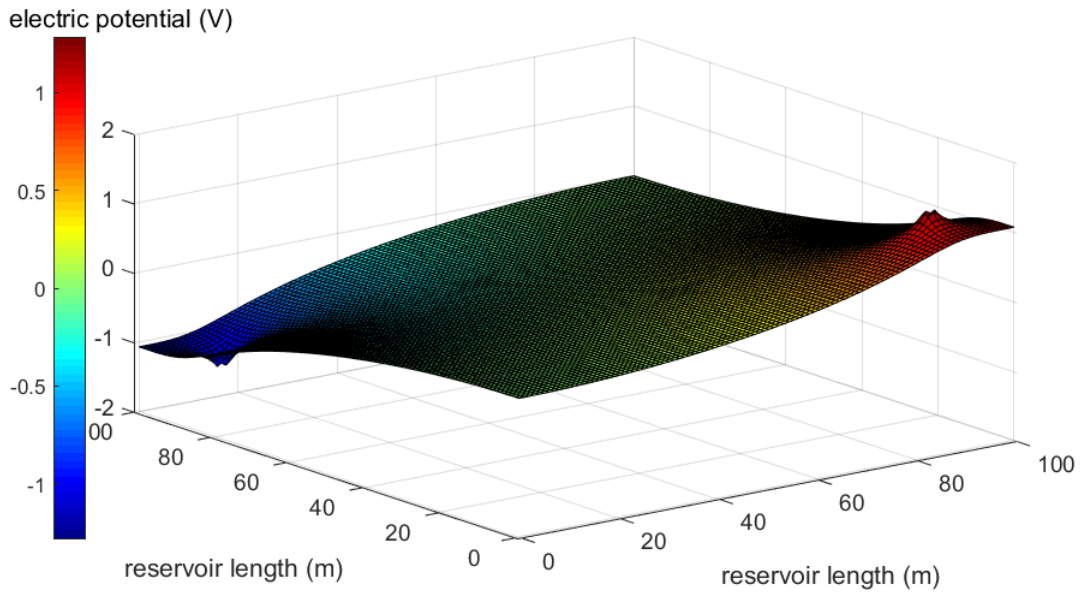

Figure 3.3: Analytical solution of electric potential in two-dimensional rectangular domain

electric current rate specified at -1 ampere. The electrical conductivity of the medium in the domain was homogeneous and had value of $1 mhos.m^{-1}$.

The numerical approximation to the solution of this two-dimensional homogeneous rectangular domain is shown in Fig. 3.4. The result of the analytical solution to the electric potential of this domain is shown in Fig. 3.3. We see there are no distinct differences between the electric potential distribution for both solutions. To get a quantitative measure of the difference, numerical solution was subtracted from the analytical solution and the result is shown in Fig. 3.5. The relative numerical error of our method was between 0 to 5 percent. To look at the numerical error from another angle, Fig. 3.6 shows the one-dimensional section of potential in a straight line between source electrode and sink electrode.

We have shown that numerical method is able to achieve comparable results to the analytical method. In practice, the analytical solution has trouble dealing with the heterogeneity of the subsurface. Fractured media are highly complex and heterogeneous, so it would be infeasible to model electric potential analytically. Thus we

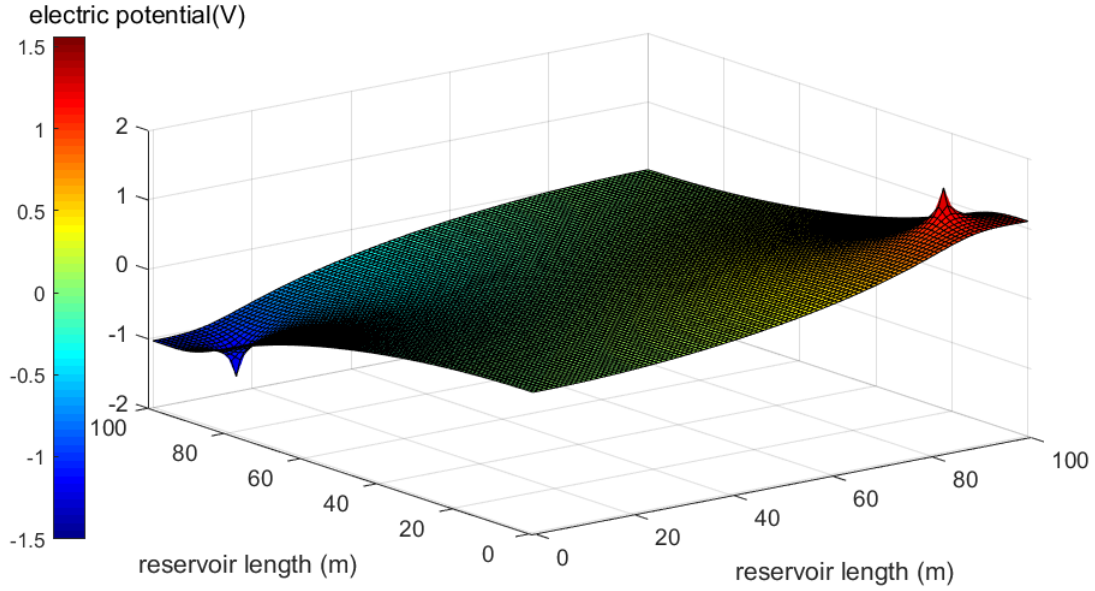

Figure 3.4: Numerical solution in two-dimensional rectangular domain

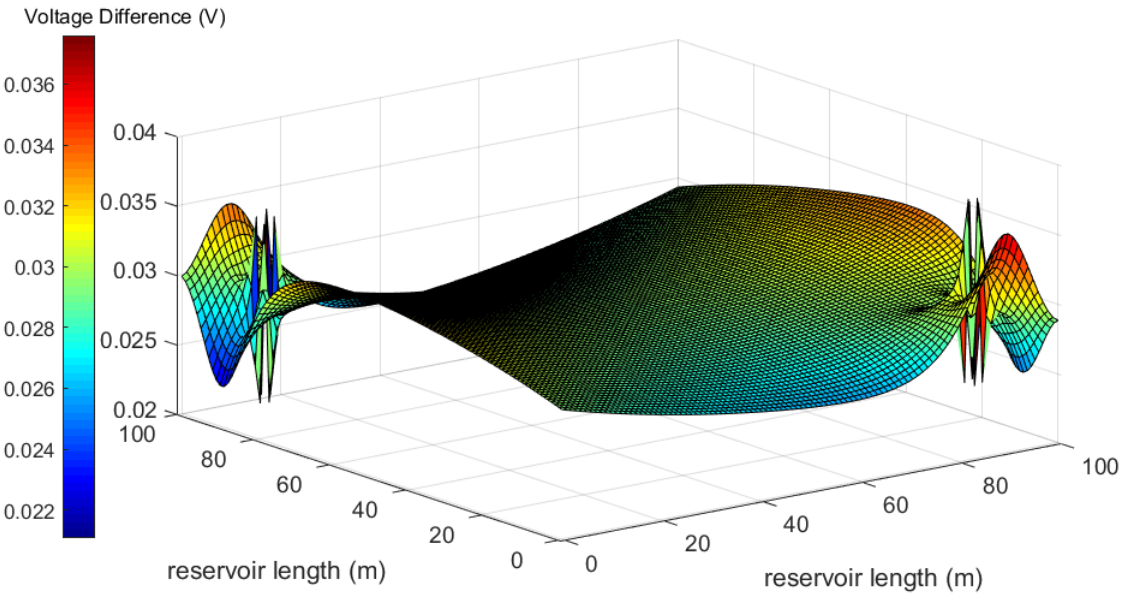

Figure 3.5: Numerical error in two-dimensional

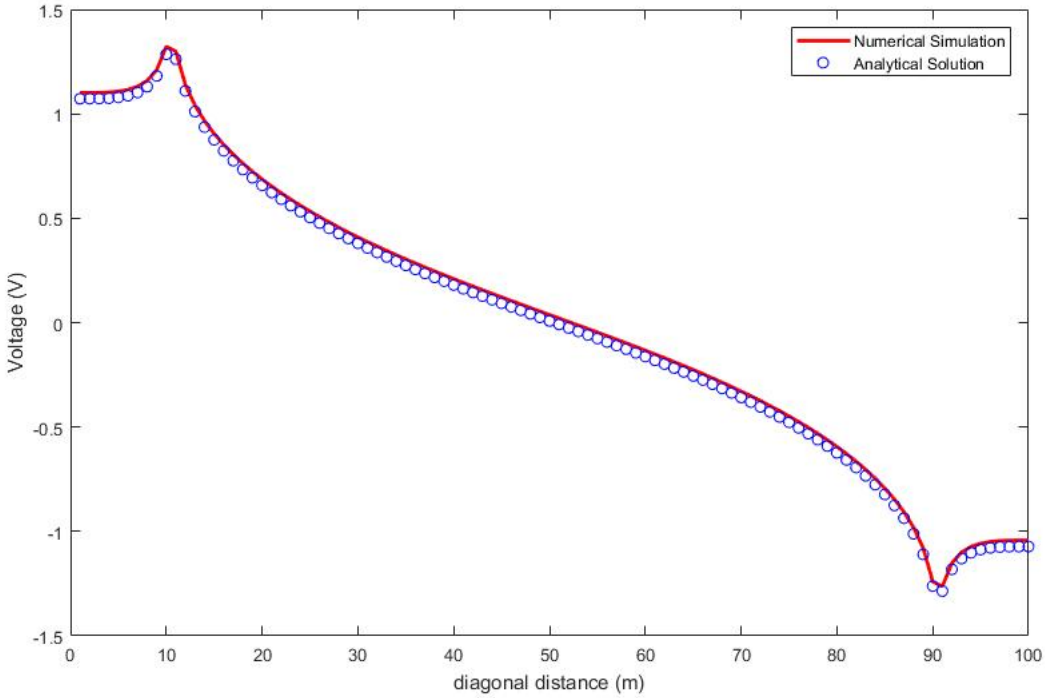

Figure 3.6: Numerical method vs. analytical method

conducted electric potential simulation using the numerical method for all scenarios throughout this study.

Chapter 4

Parameter Estimation

In this chapter we will explain how we constructed the parameter estimation framework. A complete parameter estimation framework involves a forward model, a well-defined objective function, and an effective optimization algorithm. In this study we paired electric simulation and flow simulation so that electric signals correctly reflect the dynamic change of subsurface fluid distribution. This parallel simulation was used as our forward model for parameter estimation, and we parameterized this forward model with fracture properties we were interested in, such as fracture length and fracture density. Then an objective function was defined to evaluate quantitatively how close the response of the forward model was to the measurements. Lastly we tested several optimization algorithms and determined the most effective algorithm.

4.1 Procedures for Parameter Estimation

The procedures for parameter estimation is shown in Fig. 4.1 and explained in detail below:

1. Model the real system by constructing a mathematical model. In our study this mathematical model is the paired simulation. The response generated by the real system is called measurements.

2. Input and assign initial guess of the parameters to the mathematical model.

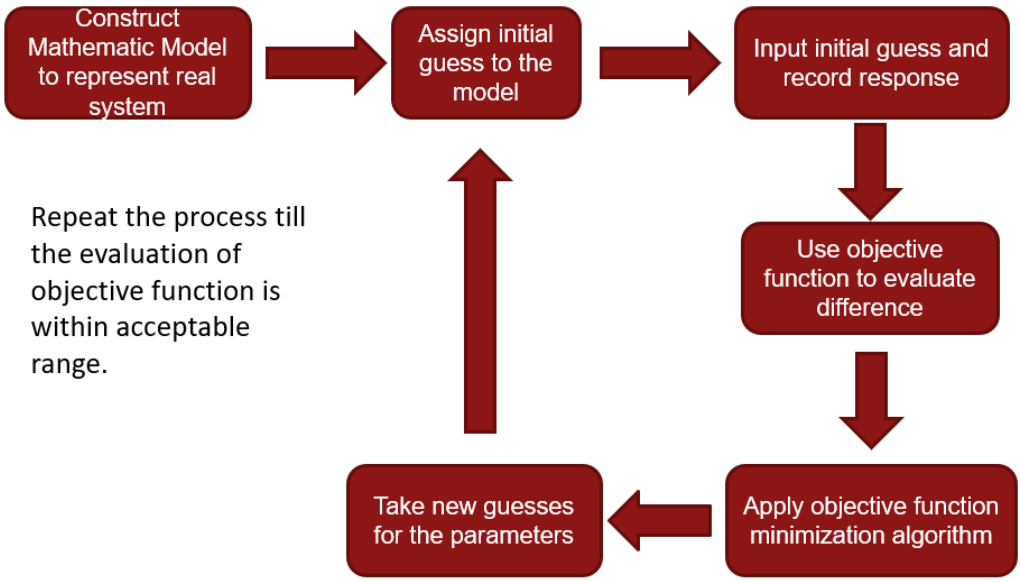

Figure 4.1: Work flow for parameter estimation

The initial guesses of the parameters need to be reasonable and are critical to the performance of optimization algorithms.

3. Input same parameters (initial guess) to the mathematical model and calculate the response.

4. Use an objective function to evaluate the difference between mathematical model response and the real system measurements. The estimation iteration stops when the objection function reaches a certain threshold and we take the parameters input as reasonable estimates for the real systems.

5. Apply the objective function minimization algorithm and iterate until the changes of estimated parameters reach a certain threshold.

6. Assign the new parameters to the mathematical model and repeat from step three to step five.

4.2 Objective Function

Once we have constructed an appropriate forward model, parametrized the model with fracture properties we wish to find, we need to find an objective function for optimization. An objective function is a mathematical function that evaluates the discrepancy between measurements and model output. By minimizing the objective function we can effectively reduce the distance between forward model and real model. Because the objective function is parameterized by the fracture properties we set, the optimization results will return estimates of the fracture properties that best describe the measured signal behavior.

In this study we chose mean-squared error as the objective function to evaluate the discrepancies between signal measurements and model output. Mean squared error function measures the average of the squared difference between two data points and has the mathematical formula described in Eq. 4.1.

$$MSE = \frac{1}{n}\sum_{i=1}^{n}(Measurement_i - ModelOutput_i)^2 \tag{4.1}$$

There are many benefits of using mean squared error to evaluate the difference between two time-lapse data series:

- Mean squared error yields the maximum likelihood estimate of the parameters that controls the objective function, assuming the errors are normally distributed.
- Mean squared error possesses desirable qualities for optimization including convexity, symmetry and differentiability (Wang and Bovik, 2009).

4.3 Optimization of Objective Function

Lastly, an optimization scheme is required to minimize the objective function and thus return the estimated fracture parameters. Optimization in practical applications is often challenging and may encounter the following problems:

- Large dimensionality.
- Functions that are not convex, thus have multiple local minima.
- Discrete feasible space.
- Nondifferential functions and constraints.
- Multiple objectives.

Optimization algorithms can be divided into two categories: gradient-based algorithms, and gradient-free algorithms. Gradient-based algorithms use the gradient of the forward function to define search directions at different steps. Examples include gradient descent method, Levenberg–Marquardt algorithm, and Boryden-Fletcher-Goldfarb-Shanno algorithm. Although gradient-based algorithms are efficient at finding local minima for high-dimensional, nonlinearly-constrained, convex problems, they often have trouble dealing with local minima in nonconvex functions. In addition, most gradient-based algorithms have trouble dealing with noisy and discontinuous functions, making them unsuitable in practical applications (Rios and Sahinidis, 2013). Gradient-free methods are not as prone to local minima as the gradient-based methods are. Most gradient-free methods mimic a heuristic approach to determine the direction of search; they are not constrained by the gradient of the function and can jump through local minima. In this study we explored several gradient-free optimization implementations and found Generalized Pattern Search method and Nelder-Mead Simplex algorithm to be the best performers in parameter estimation.

4.3.1 Generalized Pattern Search

The pattern search optimization algorithm was first introduced by Hooke and Jeeves in 1961 and this method uses a search move and polling move to determine the best optimization direction at each iteration (Hooke and Jeeves, 1961). The pattern search is a heuristic search algorithm and does not require information about the gradient of a function to find a descending or ascending direction. This gradient-free property of

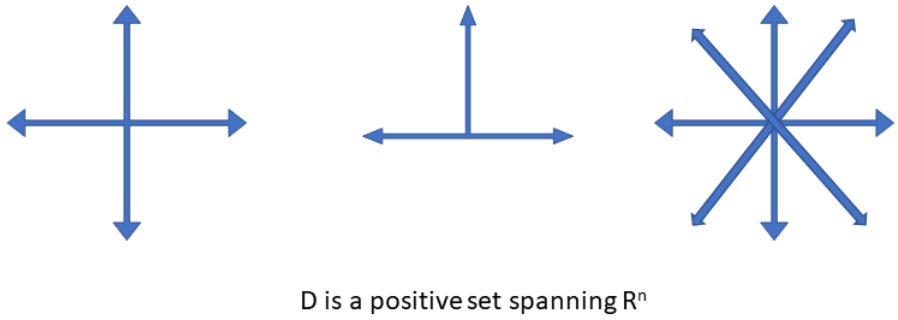

Figure 4.2: Examples of positive spanning set D

heuristic search algorithms is very useful when using simulation as the forward model. Many efforts have been made to improve the original pattern search algorithm over the years, and some of the most successful include Generalized Pattern Search (GPS) algorithms and Mesh Adaptive Direct Search (MADS) (Audet et al., 2008). Despite many variations in the extensions to the original pattern search, all the algorithms in Generalized Pattern Search and Mesh Adaptive Direct Search utilize the concept of search and poll. Let us take a detailed look.

Let x_k be a guess of the parameter we are looking for, D be a set of positive spanning directions in R^n as shown in Fig. 4.2, where R^n is the dimension of the search space, and M be the mesh grid. The size of the mesh is determined by the mesh size parameter Δ_k, and mesh size update is determined by the rule:

$$\Delta_{k+1} = \tau^{\omega_k} \Delta_k \tag{4.2}$$

where $\tau > 1$ is a constant remains the same throughout the optimization process. $\omega_k \leq -1$ if the mesh needs to be refined, and $\omega_k \geq -1$ if the mesh needs to be coarsened.

- Search move: The search move is initiated by generating a mesh grid M with a finite number of mesh points around the current parameter guess x_k. The objective function is then evaluated at all of the points on this mesh grid. If

there are points that yield better objective function values, the incumbent best point is replaced by the point on the mesh grid that has the best objective function value. The search move is at global scale and it can be visualized in Fig. 4.3(a).

- Poll move: If search move fails to generate a new guess that improves the objective function, then the algorithm moves on to the poll move as shown in Fig. 4.3(b). The poll set is constructed by a positive spanning matrix D_k formed by the columns of direction set D. The poll points in the poll set neighbor the current parameter guess x and are in the directions of D:

$$\{x_k + \Delta_k d : d \in D\} \tag{4.3}$$

  If the poll move fails to find a point that improves objective function value, then the algorithm refines the grid by applying the rule described in Eq. 4.2. Otherwise the algorithm coarsens the grid by following the same rule described in Eq. 4.2.

Torczon analyzed Generalized Pattern Search in 1997 and showed GPS frame work and convergence theory could be used for bound constrained optimization (Torczon, 1997). Bound constrained optimization is an interest to this study because of three convenient properties:

1. Bound constrained optimization effectively limits the search space and reduces the number of iterations and time needed to converge to the right solution.

2. A smaller search space can help the search process by avoiding unnecessary local minima or maxima and thus have a better chance to converge to a global minimum or maximum.

3. Bound constrained optimization works well with a simulation forward model, because optimization can not generate unrealistic guesses that cause the simulation to crash.

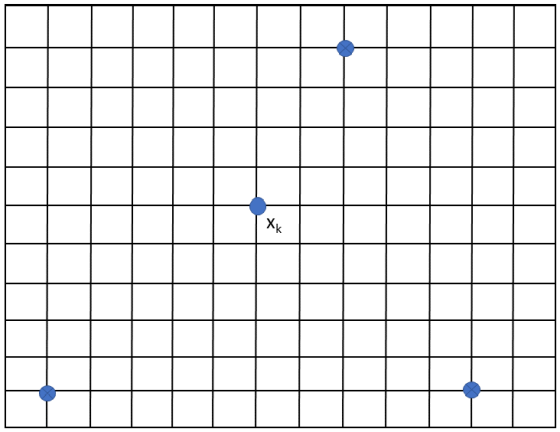

(a) Global Search

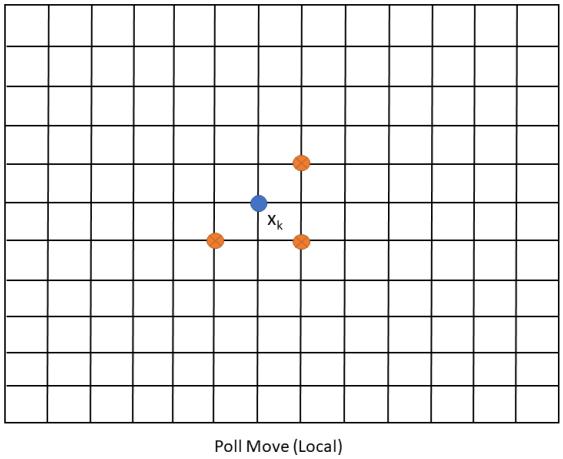

(b) Local Poll

Figure 4.3: Two steps of Generalized Pattern Search

In practice we may not have much information about fracture length or fracture density. But we know fracture length can never be negative, and we can have a realistic estimate of the ceiling of fracture length by combining geological information with injection pressure. By setting up lower bound constraints and upper bound constraints on the parameter values, the search process can effectively avoid many unnecessary searches. Thus, having appropriately defined bound constraints is critical to a successful optimization problem.

4.3.2 Nelder-Mead Simplex Algorithm

The Nelder-Mead Simplex algorithm uses a simplex structure to perform heuristic search in n-dimensional space. A simplex, sometimes called hypertetrahedron, is a structure in n-dimensional space composed of n+1 vertices. The Nelder-Mead algorithm keeps a simplex of points at each iteration. The objective function is evaluated at each of these vertices in the simplex, and subsequently three key vertices are determined to assist heuristic search: the vertex with the best objective function value, the vertex with the second best objective function value, and the vertex with the worst objective function value. The heuristic search component of Nelder-Mead algorithm is formed by five main operations: reflection, expansion, outside contraction, insider contraction and shrinking. The five operations are explained in detail below.

Let x_1, x_2 and x_{worst} denote the best vertex, the second best vertex, and the third best vertex respectively. We first calculate the average value of all vertices excluding the worst vertex. This average value is denoted as x_{avg} and it plays an instrumental role in the subsequent operations. There are a total of five simplex search operations:

- Reflection: The direction from x_{worst} to x_{avg} is a descend direction, so reflect x_{worst} on x_{avg} to get a new point. The reflection operation can be done by:

$$x_{reflection} = x_{avg} + \alpha(x_{avg} - x_{worst}) \tag{4.4}$$

- Expansion: If the reflection point is better than the best point x_1, then the direction from x_{worst} to $x_{reflect}$ is a correct descending direction, and we can

expand further:

$$x_{expansion} = x_{reflection} + \gamma(x_{reflection} - x_{avg}) \tag{4.5}$$

- Inside contraction: If the reflected point $x_{reflect}$ is somehow worse than the worst point x_{worst}, a better point is assumed in between the worst point x_{worst} and the average point x_{avg}:

$$x_{incontract} = x_{avg} - \beta(x_{avg} - x_{worst}) \tag{4.6}$$

- Outside Contraction: If the reflected point $x_{reflect}$ is not worse than the worst point x_{worst} but better than the second best point x_2, then seek the new point between the reflection point $x_{reflect}$ and the average point x_{avg}:

$$x_{outcontract} = x_{avg} + \beta(x_{avg} - x_{worst}) \tag{4.7}$$

- Shrinking: If all of the operation described above fail to find a point in the descending direction, then we shrink all of the vertices of the simplex except the best point x_1. The other vertices can be obtained by performing this mathematical calculation:

$$x_i = x_1 + \rho(x_i - x_1) \tag{4.8}$$

The geometric representation of these five operations can be visualized in Fig. 4.4. At each iteration the Nelder-Mead algorithm performs some of these five operations to the simplex and replaces the worst vertex with a new vertex. The simplex will keep rolling in the descending direction until a convergence threshold is met.

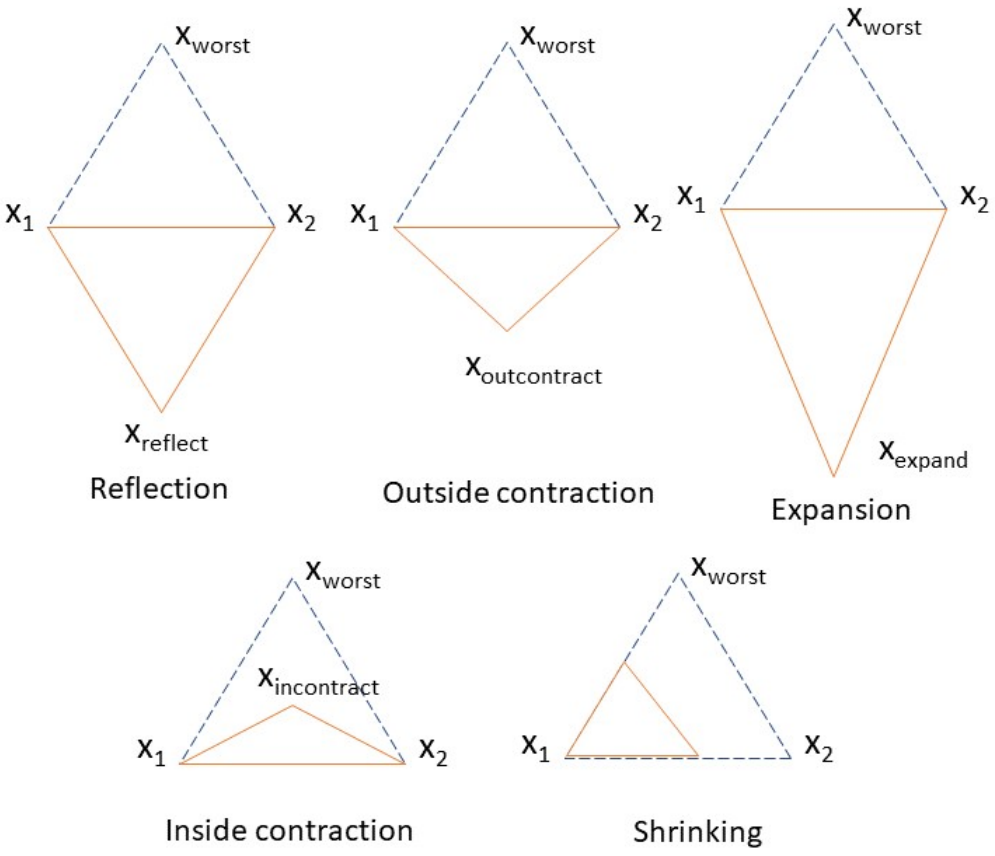

Figure 4.4: Five operations of Nelder-Mead Simplex Method

Chapter 5

Implementation

We began the implementation of the parameter estimation framework on a two-dimensional reservoir model with only horizontal flow. The discrete fracture modeling was not implemented on this horizontal flow model, so grid width and permeability field were modified to mimic properties of hydraulic fracture. The water distribution of the reservoir after 5 hours of constant injection can be visualized in Fig. 5.1, where water is injected at the edge of the reservoir near the yellow region on the right. The advantage of this model is the simplicity of implementation and low computation cost. However, the limitation of the model is also severe, as changing fracture properties other than fracture length has proven to be challenging. Multiple experiments and scenarios were conducted to confirm the functionality of purposed parameter estimation framework before we switched to a discrete fracture model.

The implementation of discrete fracture modeling is more complex, and more computationally expensive. However, discrete fracture model offers a more realistic modeling of hydraulic fractures, and allows better parameterization of hydraulic fracture specific properties. In this chapter we will focus on the details and challenges we faced while implementing discrete fracture modeling in the parameter estimation framework. For discrete fracture modeling, reservoir model construction and grid generation was done through Gmsh, a three-dimensional finite element mesh generator with a built-in CAD engine and post-processor (Geuzaine and Remacle, 2009). The reservoir model parameters are listed in Table. 5.1, the fracture parameters are listed

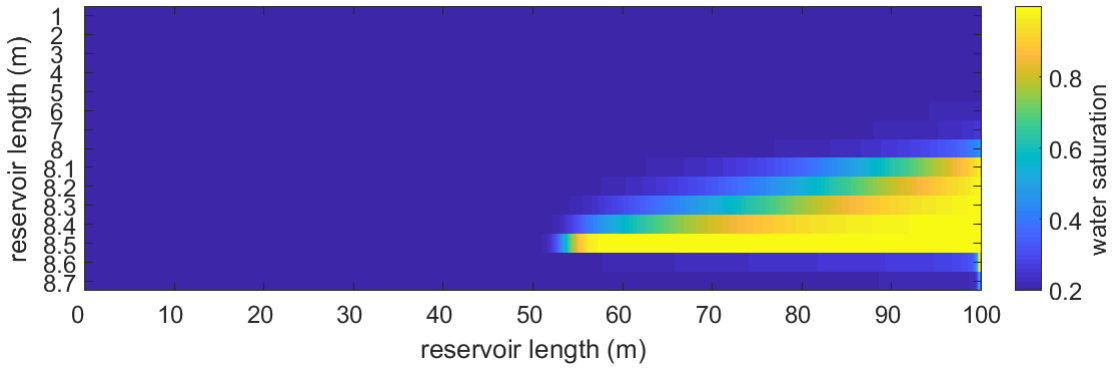

Figure 5.1: Two-dimensional horizontal flow reservoir model

Table 5.1: Reservoir Model Parameters

Property	Quantity	Units
Initial Water Saturation	0.2	N/A
Initial Oil Saturation	0.8	N/A
Initial Reservoir Pressure	3100.0	psi
Reservoir Temperature	372.22	K
Reservoir Length and Width	60.0	meter
Rock Porosity	0.2	N/A
Rock Permeability	1.0	millidarcy
Simulation Time	0.4	hour

in Table. 5.2, and the electric model parameters are listed in Table. 5.3. Reservoir scale and simulation time were all scaled down due to computation power constraint.

Table 5.2: Fracture Parameters

Property	Quantity	Units
Fracture Porosity	1.0	N/A
Fracture Permeability	1000.0	millidarcy
Fracture Length (Full)	0 - 60.0	meter

Table 5.3: Electric Model Parameters

Property	Quantity	Units
Rock Conductivity	0.1	mhos·m^{-1}
Water Conductivity	20.0	mhos·m^{-1}
Oil Conductivity	1.0	mhos·m^{-1}
Electrode Voltage	15.0	voltage
Electrode Diameter	0.025	meter

5.1 Unstructured Grid Model

As mentioned before in the second chapter, the motivation to use an unstructured mesh grid to represent fractured media was to capture the randomness of fracture generation, and the heterogeneity, discontinuity and anisotropy of fractured media. For both implementations, any changes to the geometry of the model such as fracture length change and mesh grid size change required new generation and reconstruction of the simulation model mesh grid. Mesh grid construction in an unstructured implementation is stochastic, meaning the triangle grids in the model may have different orientations, sizes and areas. This stochastic property of the unstructured implementation is acceptable in many applications, and may even be favorable in applications such as fracture modeling. However, this stochastic property proved to be quite disruptive in our application in which strict location measurements are required.

Fig. 5.2 illustrates an implementation of unstructured grid model with two fractures. To evaluate the impact of stochastic mesh generation on data measurements, we conducted 20 simulations with the same model parameters but different mesh sizes. The measurement locations were fixed at the potential measurement electrode locations indicated in Fig. 5.2, and pressure, electric potential were recorded at these two locations in all 20 simulations. Fig. 5.3 shows the pressure measurements for each simulation, Fig. 5.4 shows the electric potential measurements for each simulation, and Fig. 5.5 shows the objective function evaluation for each simulation. We can observe obvious differences among the measurements from different simulations. As a result, the objective function values are variably distributed which makes it impossible for any optimization scheme to succeed. Thus we concluded that unstructured

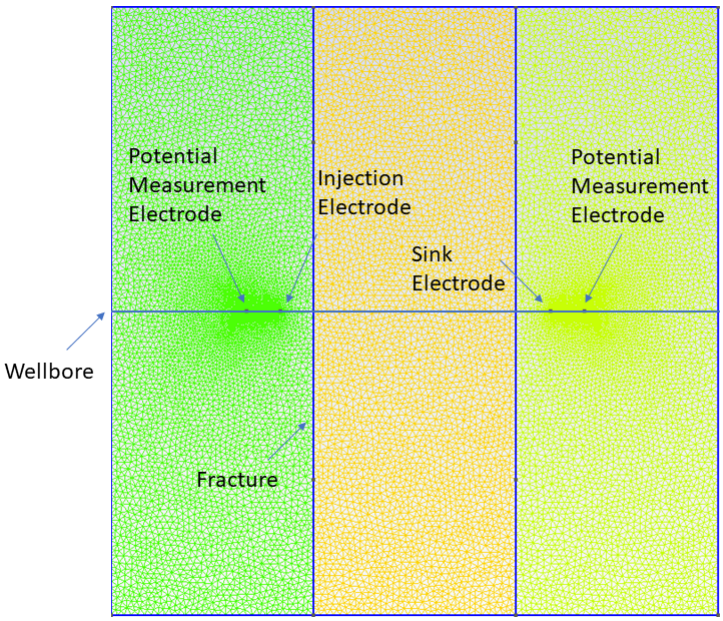

Figure 5.2: Unstructured implementation

implementation was not ideal for the purposed parameter estimation framework in this study.

5.2 Structured Grid Model

The structured grid model implementation is straightforward. Without stochastic mesh grid generation for forward simulation at each parameter guess, the objective function evaluations were consistent and allowed the optimization algorithm to find paths to descend. Fig. 5.6 illustrate an example of the implementation of structured grid model with 11 fractures. We see all the grid blocks are distributed uniformly and have the same size and shape. In fact, the structured models we deployed in this study were constructed by forcing triangle grids into the same shape. This structured implementation was integrated successfully into our parameter estimation framework to conduct further experiments.

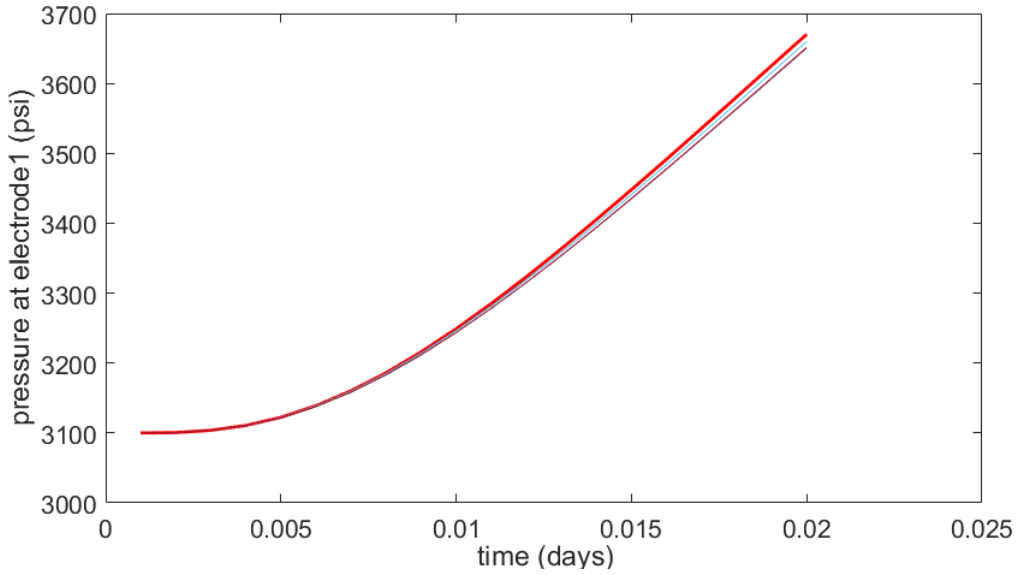

(a) Pressure at measurement point 1

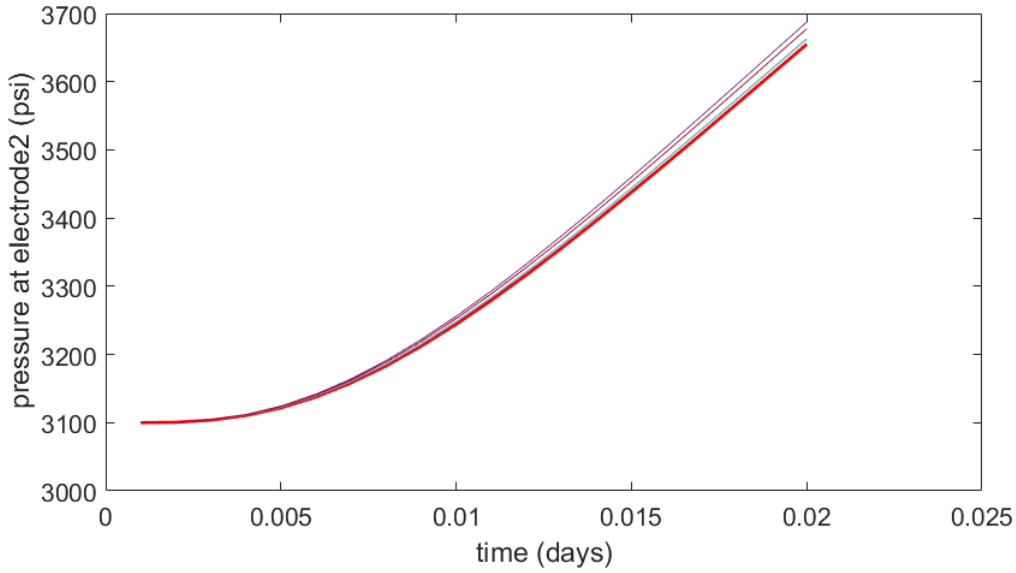

(b) Pressure at measurement point 2

Figure 5.3: Pressure recordings at measurement points 1 and 2 for 20 simulations using different mesh sizes

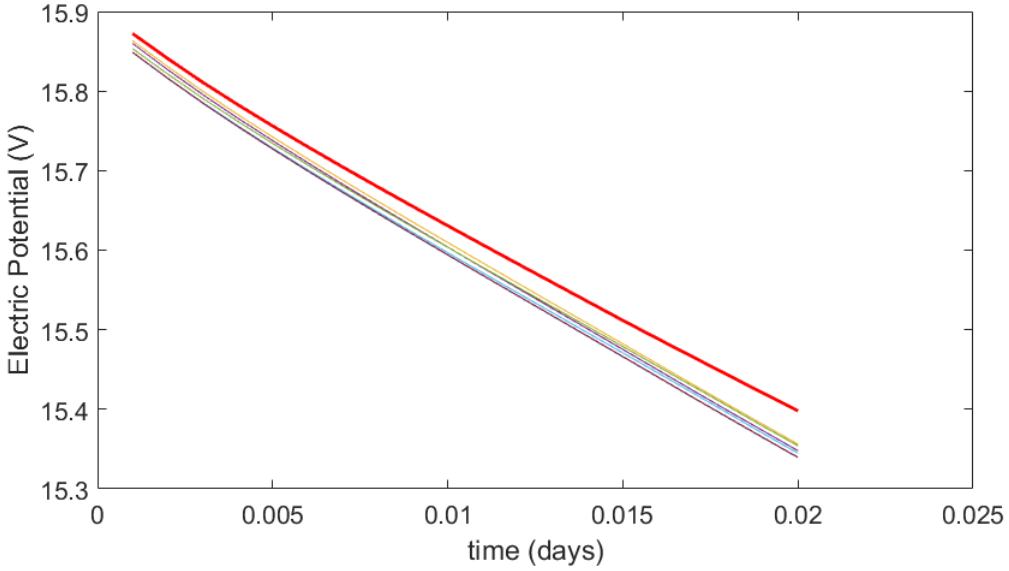

Figure 5.4: Electric potential recordings between measurement points 1 and 2 for 20 simulations using different mesh sizes

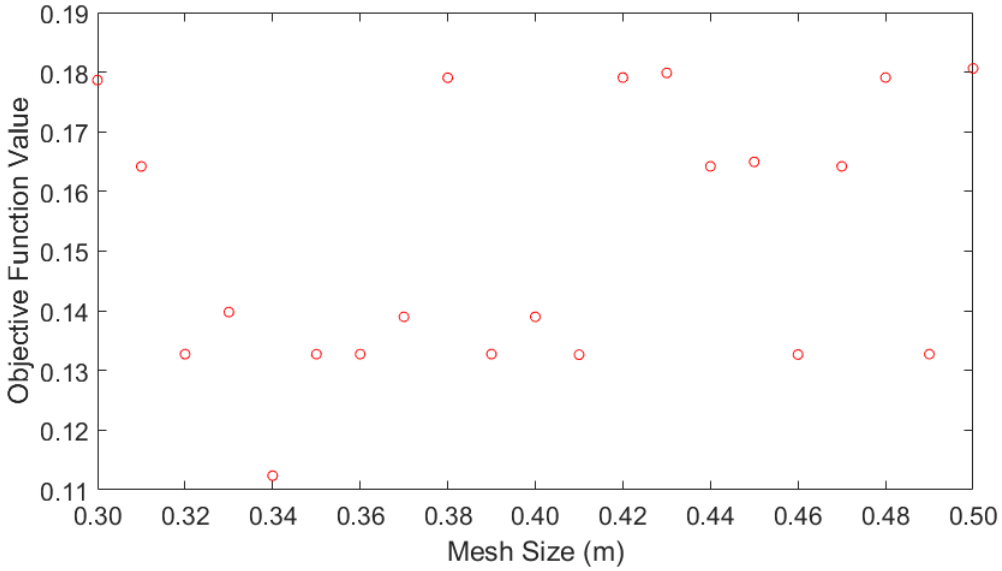

Figure 5.5: Objective function evaluations of 20 simulations using different mesh sizes

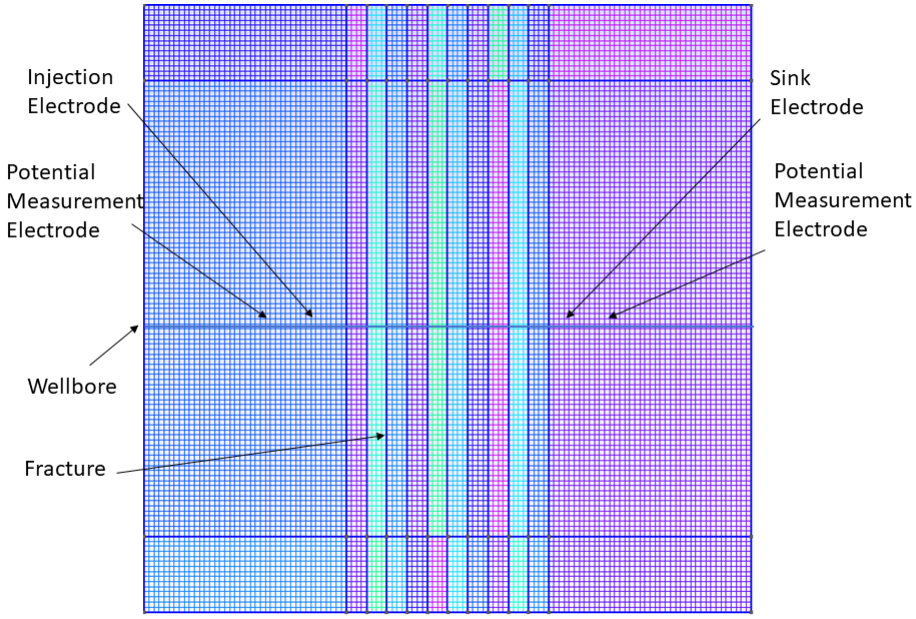

Figure 5.6: Structured Implementation

Chapter 6

Sensitivity Analysis

In this study we identified some of the most important factors in analyzing time-lapse resistivity data, and conducted sensitivity analysis on these factors to examine their impact.

6.1 Location Sensitivity

To evaluate the sensitivity of parameter estimation performance on locations, we fixed all the simulation parameters to be constant so that all the evaluations at different location combinations were fair. Fig. 6.1(a) best describes the process. The yellow dots in the figure indicate source and sink electrode, and the red dots in the figure indicates measurement locations. In our analysis the source electrode on the left was fixed at the same location, and the sink electrode was moved to different locations along the wellbore. At each location the fracture length was changed by a constant amount and the changes of objective function values were recorded to indicate the sensitivity of electric potential signal to fracture length. The sensitivity evaluation formula can be summed up in Eq. 6.1:

$$locationsensitivity = \frac{\partial ObjectiveFunction}{\partial FractureLength} \tag{6.1}$$

Fig. 6.1(b) visualizes the result of electrode sensitivity analysis. We saw negligible sensitivity when the two electrodes were placed close to each other, as indicated on the left side of the figure. This low sensitivity was expected when the distances between electrodes were short because electrical current information could not travel far. The sensitivity increased as the sink electrode moved further and further away from the source electrode, and peaked at the wellbore section between 30 meter and 45 meters. It is worth noting that although the wellbore section between 30 meter and 40 meter experienced high electric signal sensitivity with respect to fracture length, we eventually chose wellbore location at around 43 meter as shown in Fig. 6.1(b) as the sink electrode location due to considerations of practical implementation. Installing sink electrode in the wellbore section between 20 meter and 40 meter would be infeasible because this section was the fractured zone.

6.2 Injection Fluid Electrical Conductivity Sensitivity

Water is the most commonly used fracture fluid in hydraulic fracturing operations. Table. 3.1 shows a list of resistivity of common subsurface components. Saline water has a range of resistivity depending on its salt content. In order to understand how the resistivity of injection fluid affects the performance of parameter estimation, we evaluated parameter estimation performance at different injection fluid resistivity values. In this analysis injection fluid was assumed to have similar properties to the reservoir water. We made this assumption because we envisioned the future of hydraulic fracturing would be environmental friendly, and recycling produced water for hydraulic fracturing would be the common practice.

Fig. 6.2 shows the result of electrical conductivity sensitivity analysis. The experiments were conducted in an oil-water two-phase system with signal-to-noise ratio of 50. Our purposed parameter search framework was able to estimate the correct fracture length consistently with every injection fluid electrical conductivity we specified. From this result we can conclude the current parameter search framework works

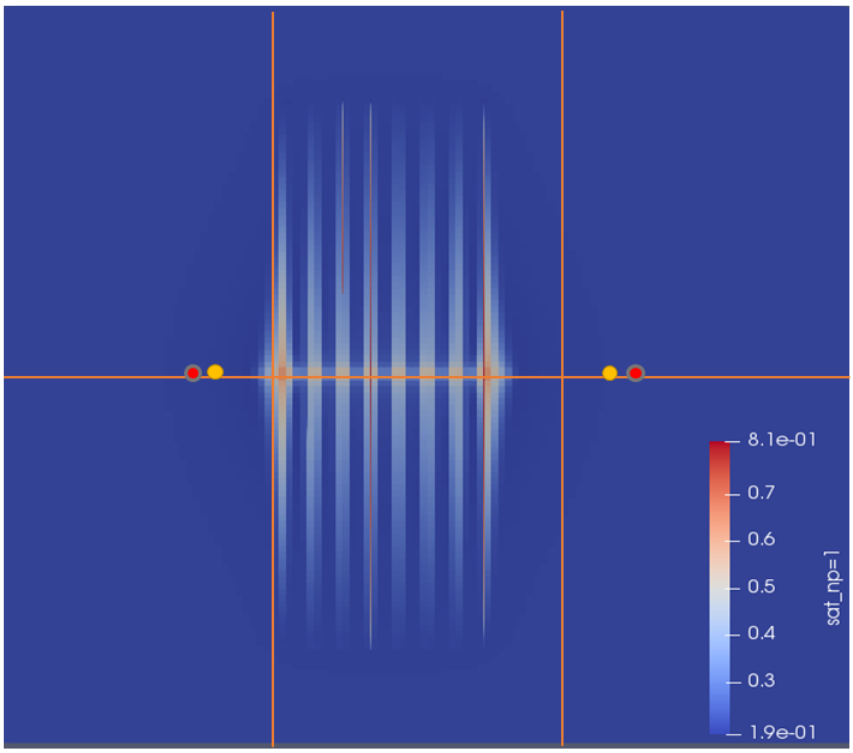

(a) Reservoir model in cross section view

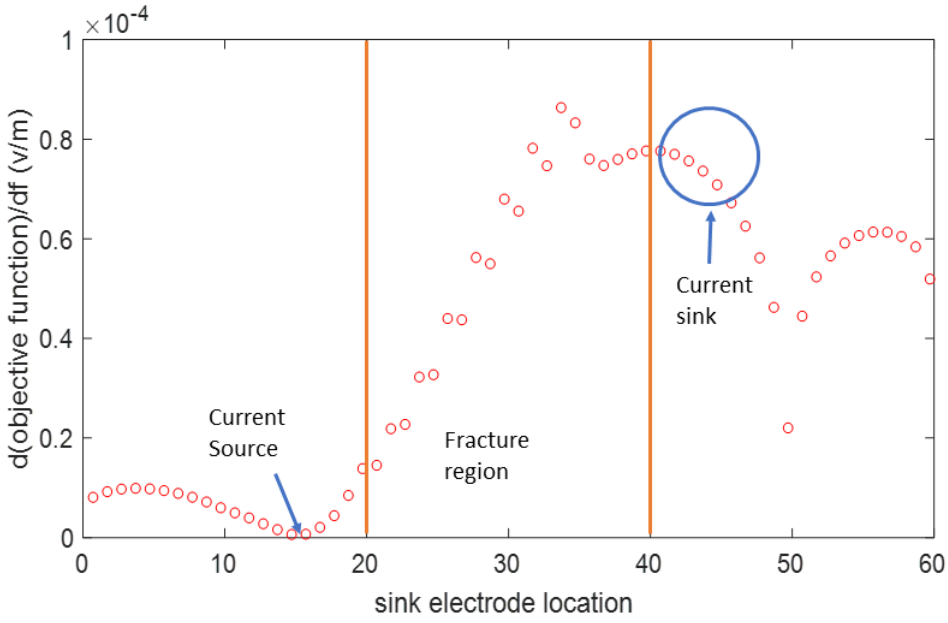

(b) Electrode location sensitivity

Figure 6.1: Electrode location sensitivity

as long the contrast between the electrical conductivity of injection fluid and the electrical conductivity of reservoir oil passes a threshold value.

Table 6.1: Resistivity of common materials

Materials	Resistivity [ohm-m]
Saline water (20%)	0.05
Saline water (3%)	0.15
Clay	5 - 150
Gravel	480 - 900
Limestone	350 - 6,000
Sandstone (consolidated)	1,000 - 4,000
Igneous rock	100 - 1,000,000

6.3 Noise Sensitivity

Electric potential measurement comes with a great deal of noise in real world applications. The sources of noise include degradation of the subsurface installation, induced polarization effects, environmental noise, etc. (Schmidt-Hattenberger et al., 2011). Fig. 6.3 illustrate some typical downhole electric potential measurements. In noise sensitivity analysis we added noise to electric potential measurements in order to test how robustly our model performs in a noisy environment.

The type of noise we added to the simulation result was additive white Gaussian noise: "additive"because noise is intrinsic to the information system, "white"means the noise is uniform power across the frequency band, and "Gaussian"means the noise has a normal distribution. We first measured the signal power of our data:

$$signalpower = 10 \times \log_{10} \|data\|^2/(datasize). \tag{6.2}$$

From the signal power of our data we calculated the noise power:

$$noisepower = 10^{\frac{signalpower}{10}}. \tag{6.3}$$

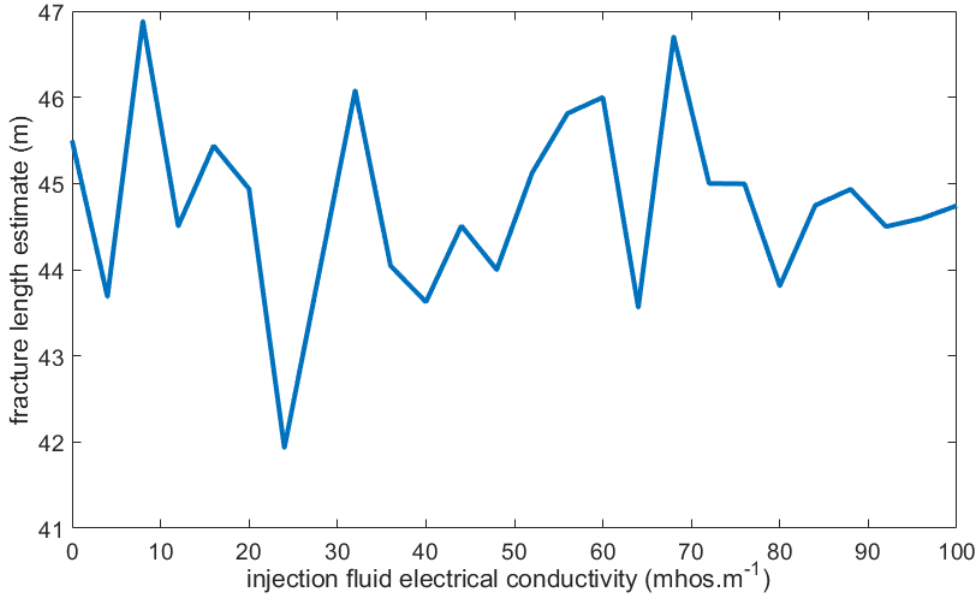

(a) Fracture length estimate

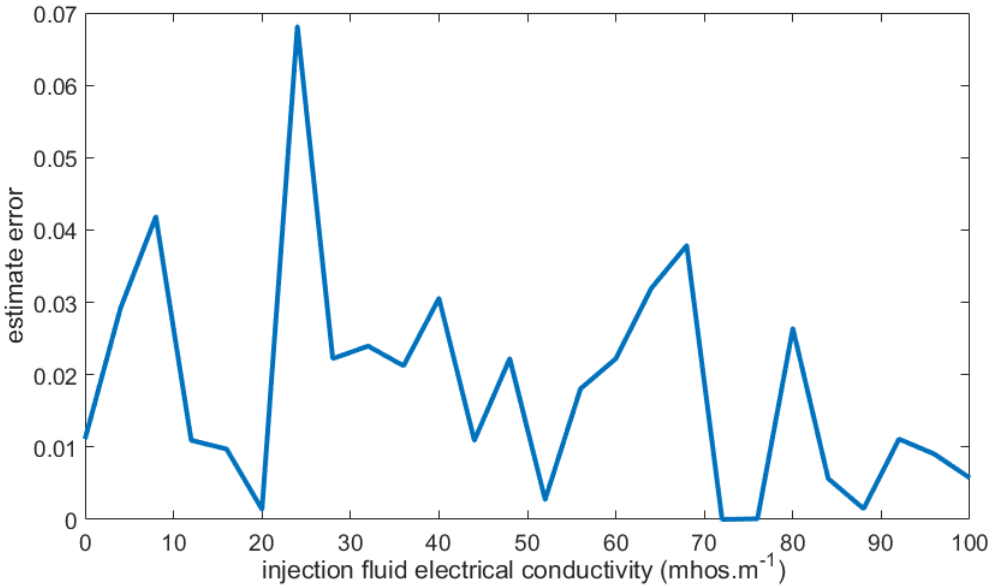

(b) Fracture length estimate error

Figure 6.2: Injection fluid conductivity sensitivity

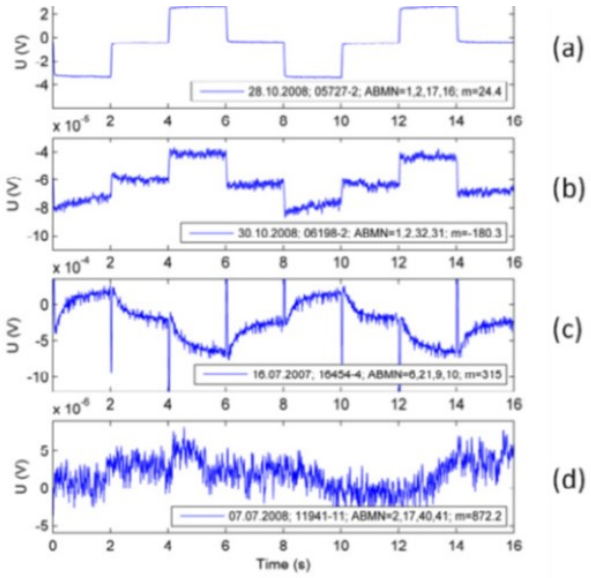

Figure 6.3: Example of typical time-lapse potential measurement (Schmidt-Hattenberger et al., 2011). Signal qualities: regular (a,b), asymptotic discharging with spikes (c), random(d).

Then we generated the Gaussian noise:

$$noise = \sqrt{noisepower} \times Gaussian(x|0,1). \tag{6.4}$$

We then tested the parameter estimation algorithm on different levels of noisy electric potential measurement to examine the impact of noise. Both Generalized Pattern Search and Nelded-Mead Simplex algorithm performed well in one parameter search scenario where the forward model was parameterized by only fracture length. As shown in Fig. 6.4 and Fig. 6.5 our parameter estimation method was able to consistently estimate the true fracture length using time-lapse electric potential signal from signal to noise ratio 100 to signal noise ratio 40. The performance of the model deteriorated when the signal to noise ratio dropped below 40 and our model could no longer make a confident estimate below that threshold.

Estimating two parameters is more difficult than estimating one parameter because the search algorithm is looking for the best objective function value in a higher dimensional space. In this study we parameterized the forward model by fracture

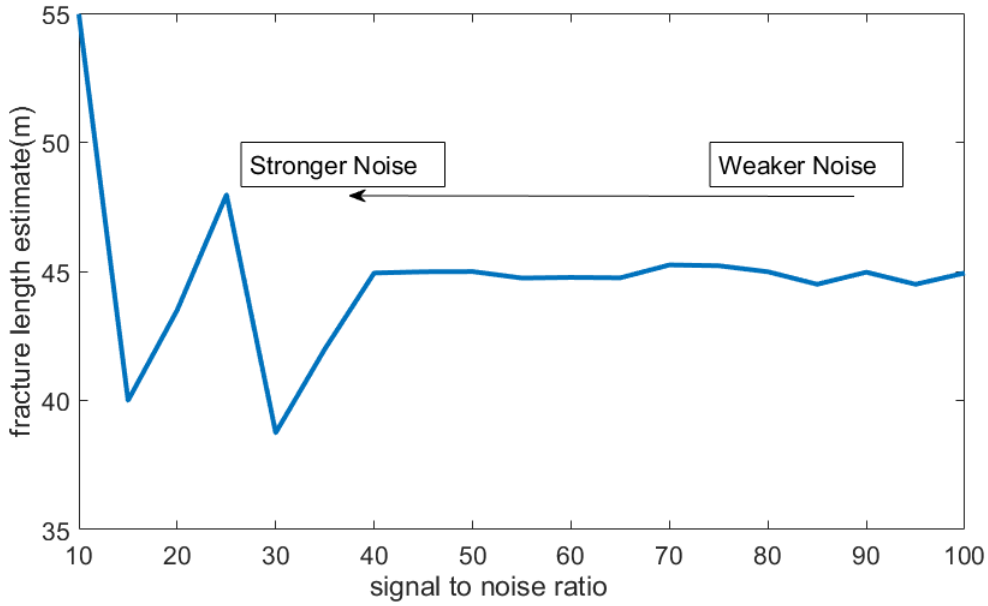

(a) Fracture length estimate

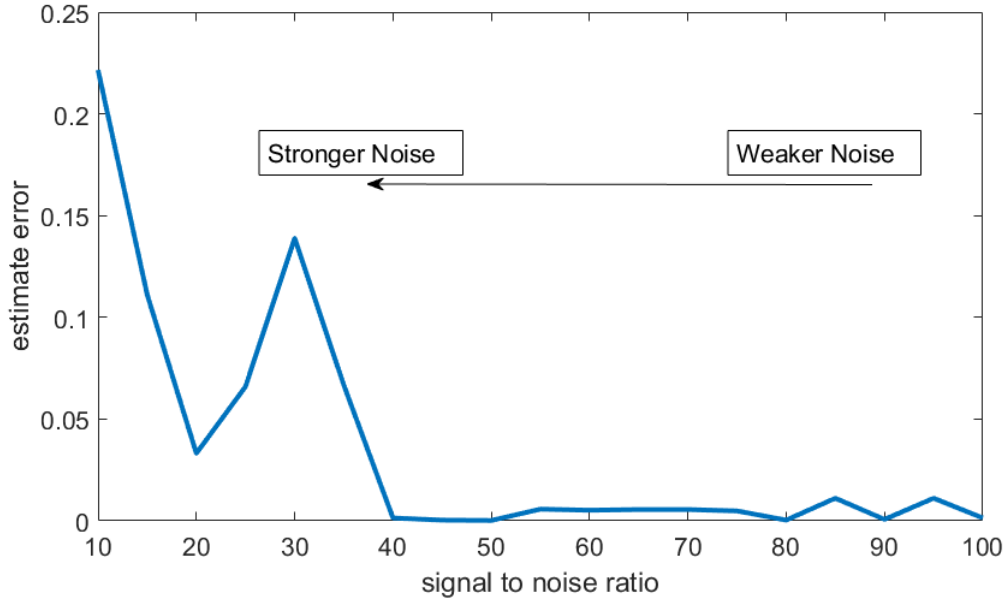

(b) Fracture length estimate error

Figure 6.4: Generalized Pattern Search performance on noisy data(one parameter search)

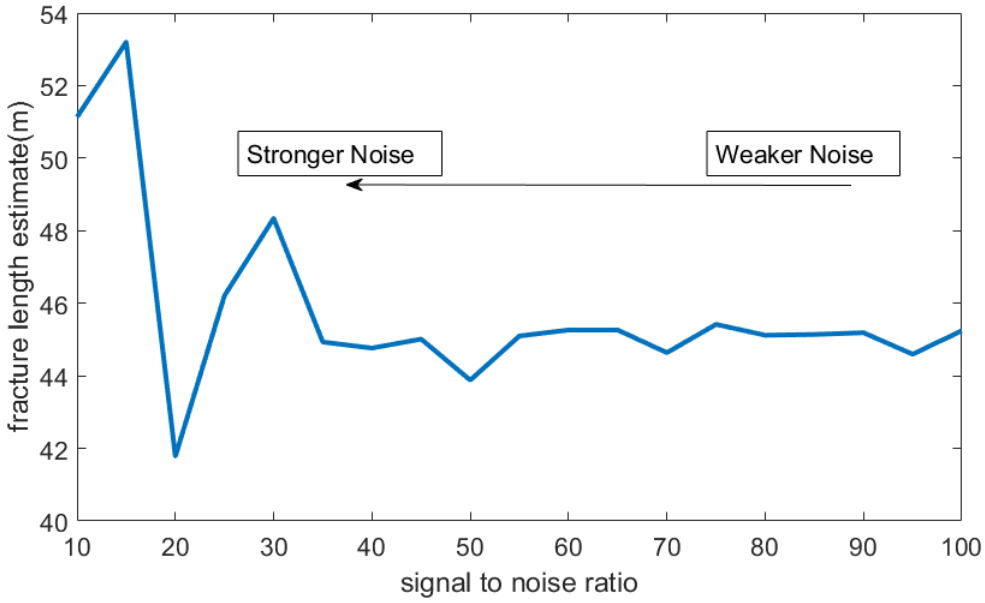

(a) Fracture length estimate

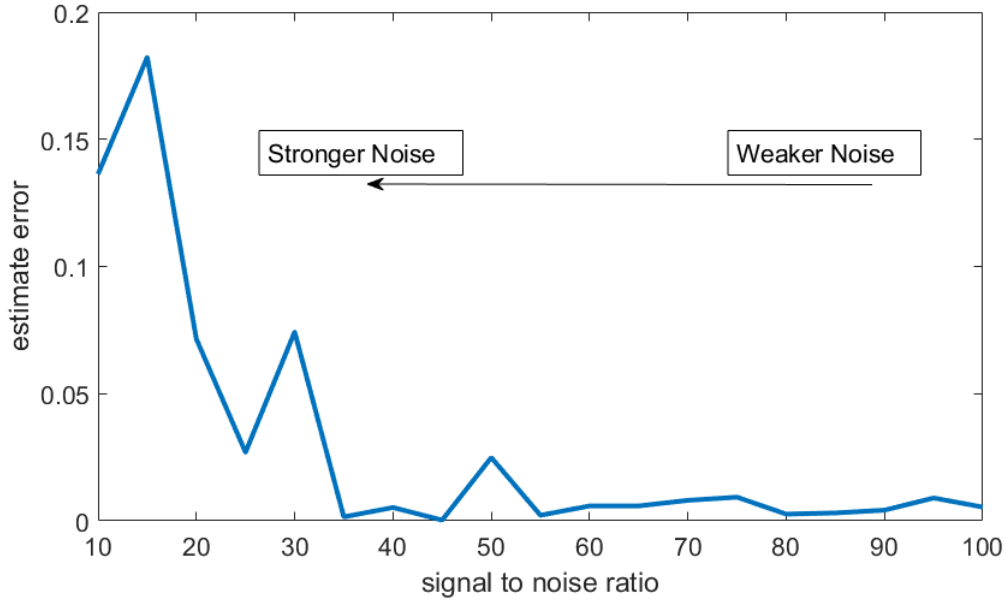

(b) Fracture length estimate error

Figure 6.5: Nelder-Mead Simplex method performance on noisy data(one parameter search)

length and fracture density, and performed parameter estimation using the framework we built. We see in Fig. 6.6 and Fig. 6.7 our parameter estimation framework with Generalized Pattern Search optimization was able to make the correct estimate of fracture length and fracture density consistently in the noisy environment, despite more challenging optimization requirement. The search time for two parameters was much longer than the search time for one parameter. Similar to the one parameter search cases, our purposed method with Generalized Pattern Search optimization was able to withstand data with signal to noise ratio down to 40 in two parameter search cases. Once the signal to noise ratio dropped below 40, our method could no longer make confident estimates. The performance of Generalized Pattern Search was acceptable in both one parameter search scenarios and two parameter search scenarios. On the other hand, Nelder-Mead Sipmlex method was only successful in one parameter search scenarios. Fig. 6.8 and Fig. 6.9 indicate that Nelder-Mead optimization can not converge to the global minimum at any noise level of the data while searching for two parameters. We will provide detailed analysis in the next chapter.

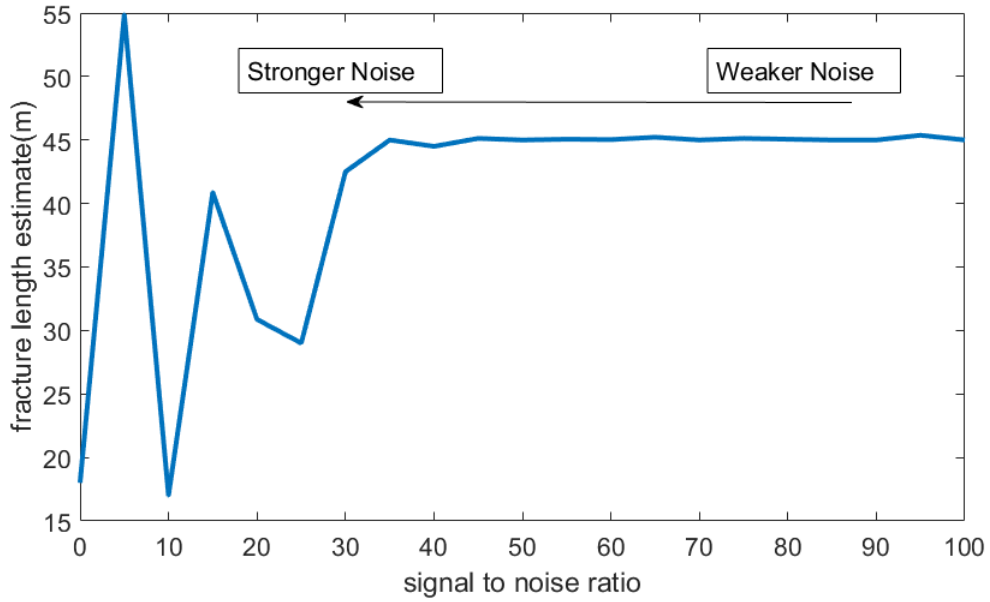

(a) Fracture length estimate

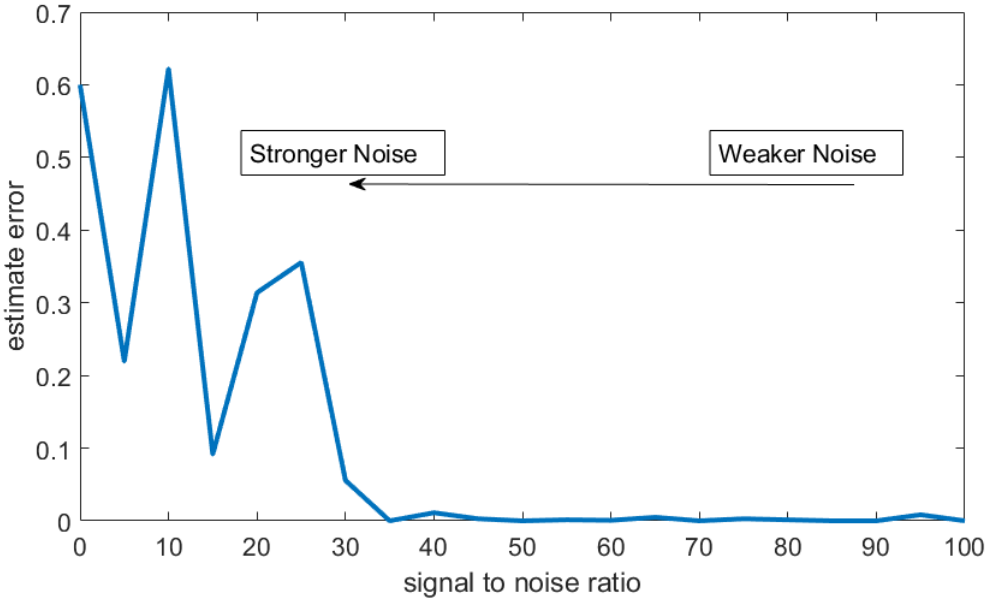

(b) Fracture length estimate error

Figure 6.6: Generalized Pattern Search performance on noisy data(two parameter search)

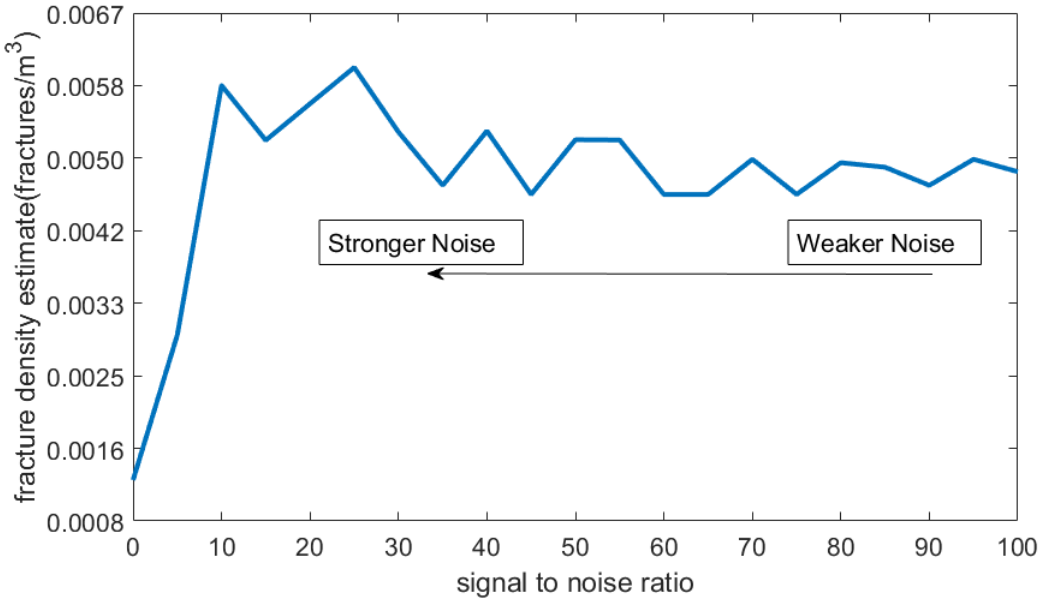

(a) Fracture density estimate

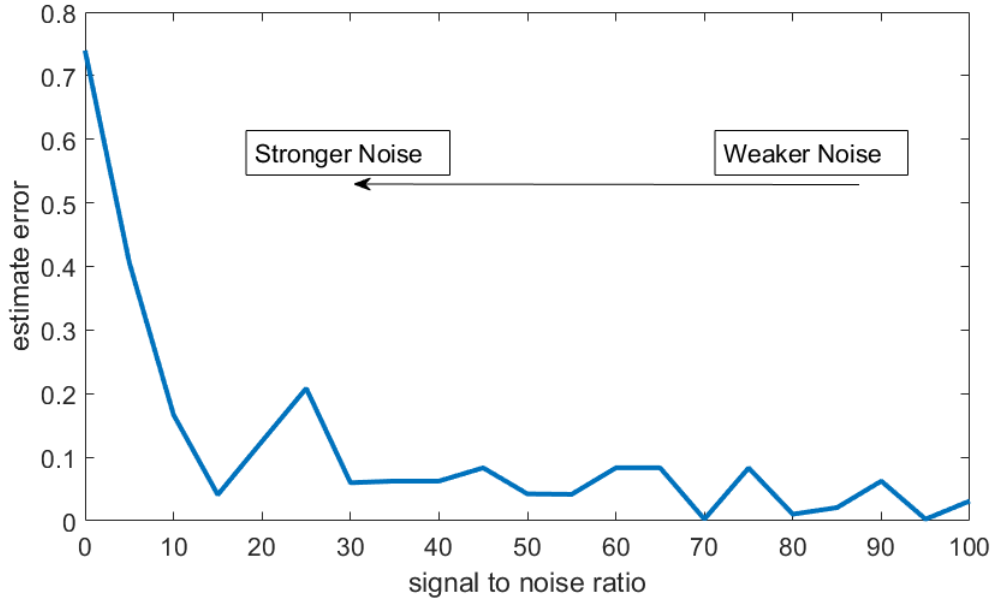

(b) Fracture density estimate error

Figure 6.7: Generalized Pattern Search performance on noisy data(two parameter search)

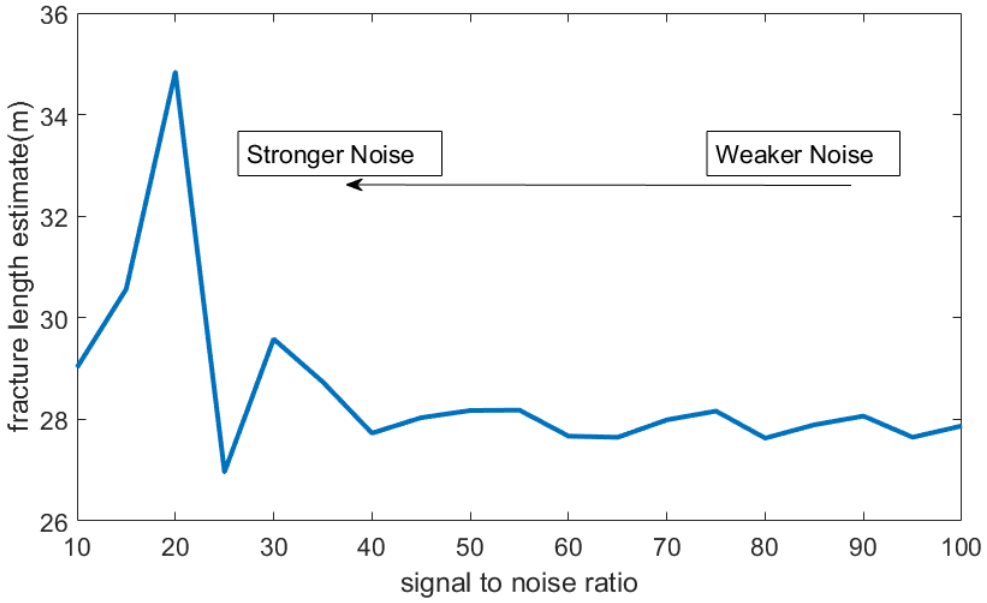

(a) Fracture length estimate

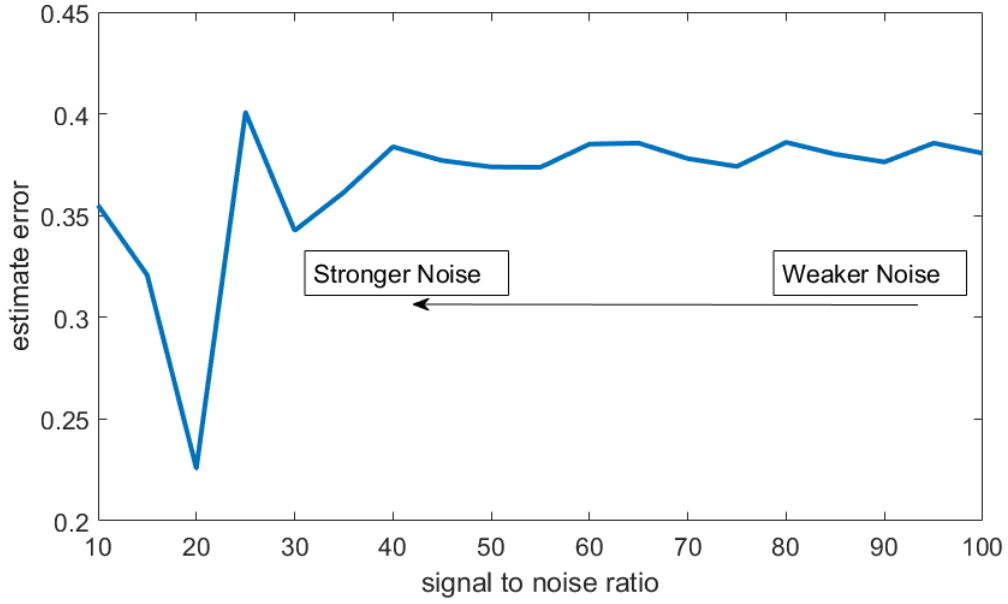

(b) Fracture length estimate error

Figure 6.8: Nelder-Mead Simplex method performance on noisy data(two parameter search)

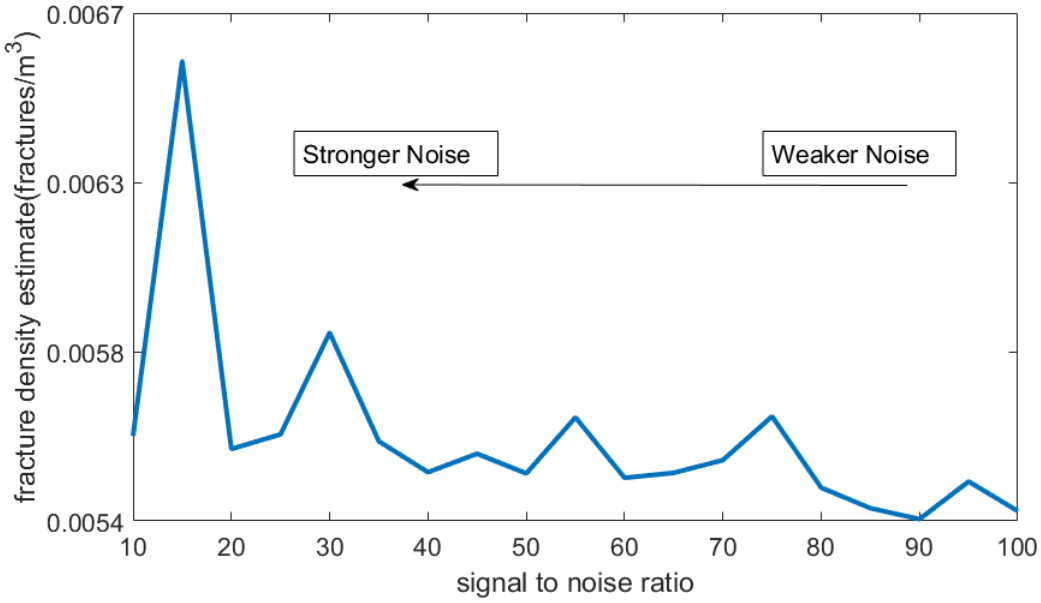

(a) Fracture density estimate

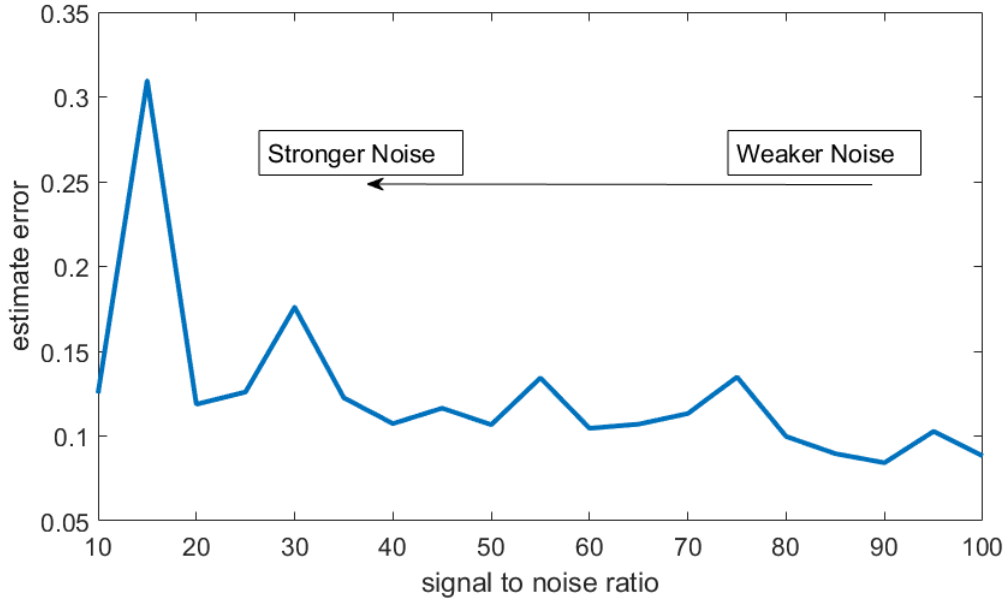

(b) Fracture density estimate error

Figure 6.9: Nelder-Mead Simplex method performance on noisy data(two parameter search)

Chapter 7

Results and Findings

In this chapter we present the findings of this study. We will first discuss the parameter estimation results for electric potential data without any noise. Then we will describe parameter estimation results for electric potential data with various levels of noise. The primary objective of this study was to build a method to estimate fracture length using resistivity data. Once we successfully accomplished estimating fracture length, we added fracture density as a second parameter to estimate. We will show the results of searching only for fracture length, and the results of searching for both fracture length and fracture density.

All of the results shown in this chapter are based on electric potential signals generated from a reservoir model with 45 *meter* long fractures and fracture density of 0.005 $fractures/m^3$ as shown in Fig. 7.1(a). The time-lapse electric potential signal is shown in Fig. 7.1(b).

7.1 Parameter Estimation Without Noise

We began our investigation by performing parameter estimation on electric potential data without any noise. For this section of the experiments we were fitting the data described in Fig. 7.1(b). In reality, noise-free data are quite rare, as systematic error and ambient environment impact are omnipresent in data measurements. Nonetheless, we tested our parameter estimation method on noise-free data so that we could

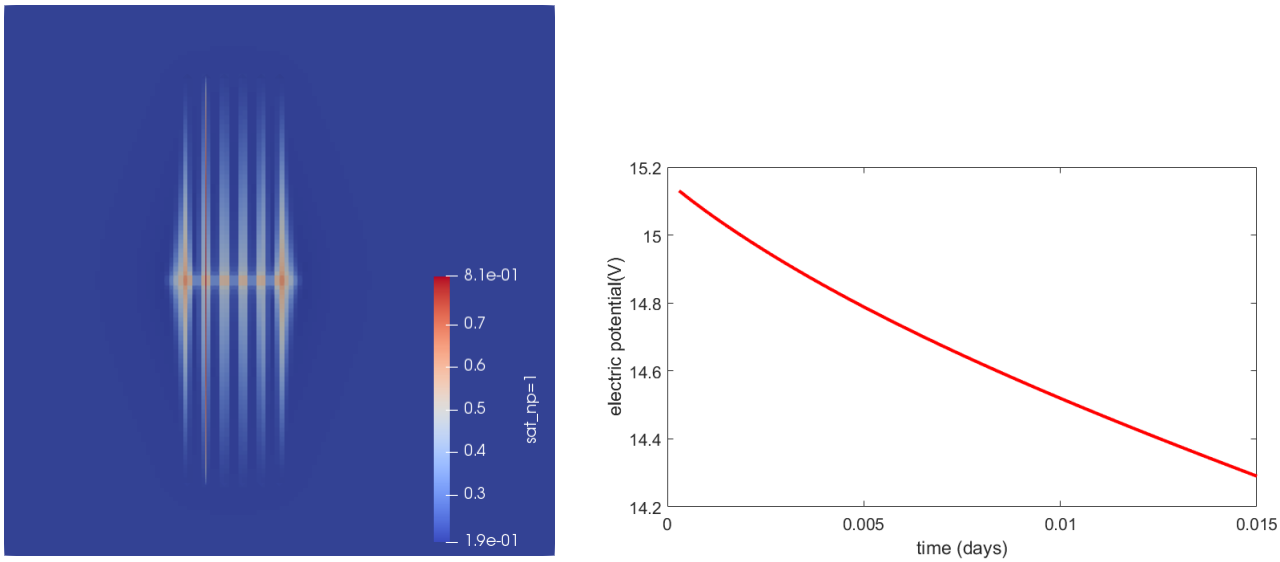

(a) Reservoir model

(b) Electric potential signal

Figure 7.1: Reservoir with $45m$ fractures and fracture density 0.005 fractures/m^3

have confidence in our approach before moving on to more complex situations.

7.1.1 Fracture Length Estimate

The results of estimating fracture length from perfectly measured data (noise-free) are shown in Fig. 7.2 and Fig. 7.3. We see that both Generalized Pattern Search and Nelder-Mead had no problem converging to the correct estimate by driving the objective function value essentially to zero within machine precision. Note that although total function evaluations shown in Fig. 7.3(b) are much more than the total function evaluations shown in Fig. 7.2(b), Nelder-Mead Simplex optimization actually converged to the correct solution faster than Generalized Pattern Search optimization. The reason Nelder-Mead method took more function evaluations was because the optimization tolerance was stricter than the optimization tolerance in Generalized Pattern Search.

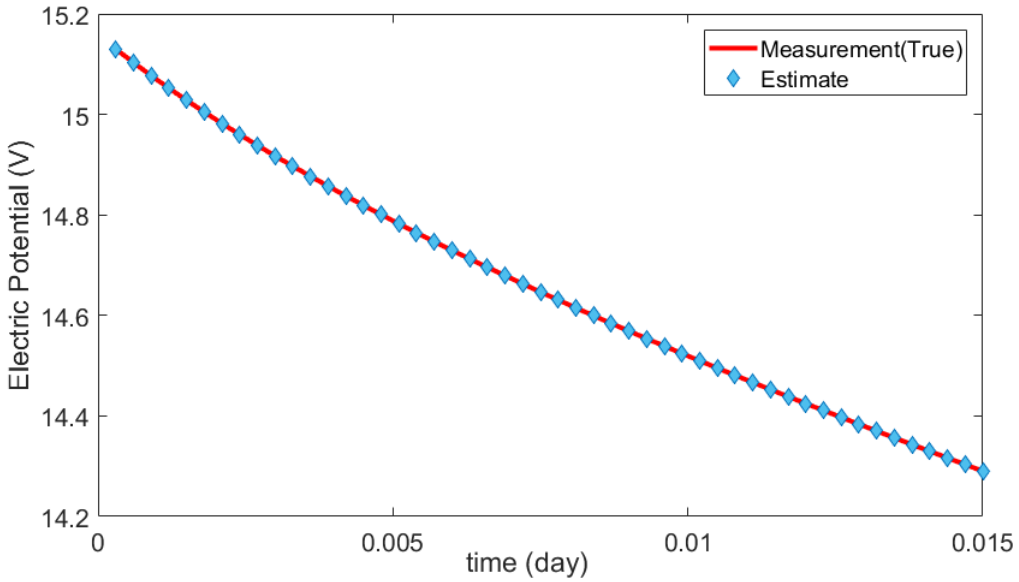

(a) Estimate of measurement data

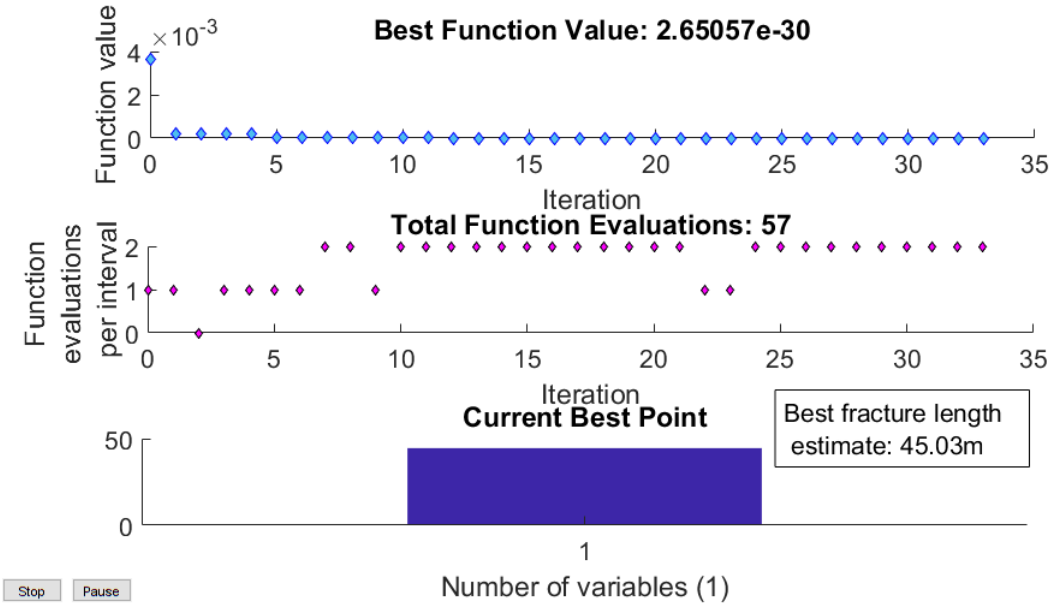

(b) Optimization information

Figure 7.2: Fracture length estimate by applying Generalized Pattern Search on perfectly measured data.

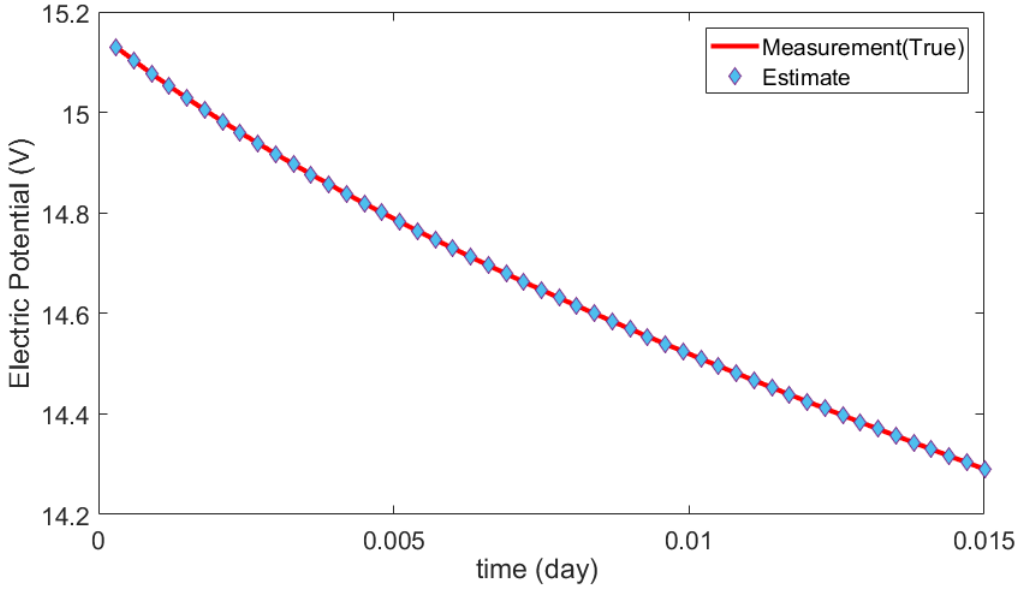

(a) Estimate of measurement data

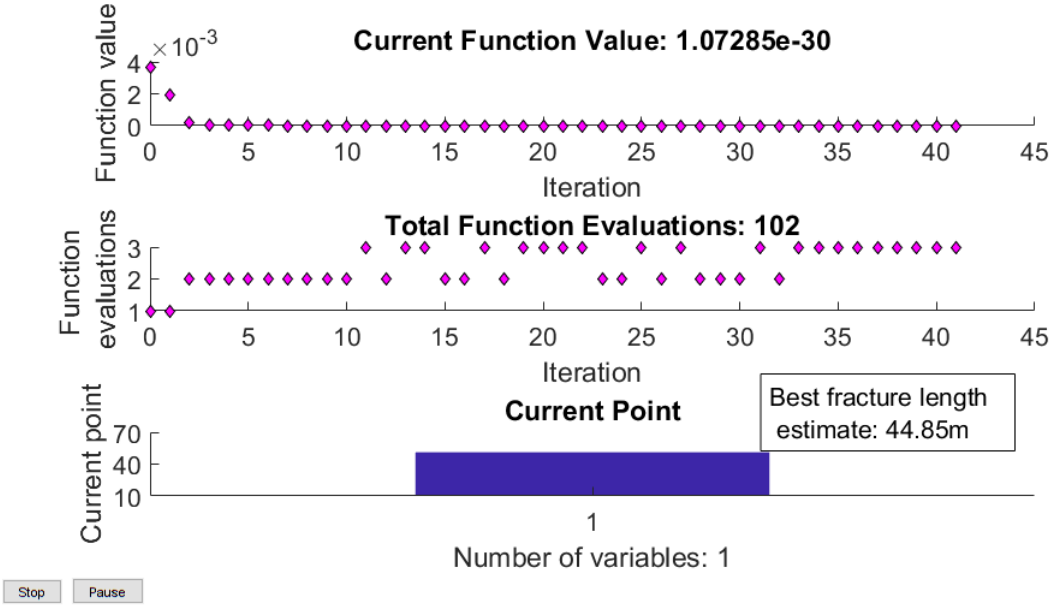

(b) Optimization information

Figure 7.3: Fracture length estimate by applying Nelder-Mead on perfectly measured data.

7.1.2 Fracture Length And Fracture Density Estimate

We mentioned in the previous chapter that estimating two parameters is a more strenuous task than estimating one parameter. In one parameter search, the Generalized Pattern Search optimization algorithm makes at most two evaluations at each iteration, and Nelder-Mead Simplex optimization makes at most three evaluations at each iteration before moving on to the next iteration. The optimization algorithm takes at most two evaluations at each iteration because Generalized Pattern Search uses a direction based optimization scheme and there are only two directions in the one-dimensional space. Nelder-Mead Simplex method makes at most three evaluations at each iteration because shrinking and inside contraction is equivalent in the one-dimensional space. There are an infinite set of directions in two-dimensional space, and thus it becomes much more challenging to find directions to decrease the objective function value. Generalized Pattern Search evaluates four of the directions in the direction set in two-dimensional space, and Nelder-Mead Simplex method performs some of the five operations (reflection, expansion, outside contraction, inside contraction and shrinking) before executing the update policy.

Fig. 7.4 shows an example of fracture length and fracture density search using Generalized Pattern search. Although the number of function evaluations was approximately twice as the number of function evaluations in the one parameter search, the algorithm was able to find the correct fracture length and fracture density while minimizing the objective function essentially to zero. Generalized Pattern Search was successful in finding the correct fracture length and fracture density, but Nelder-Mead Simplex search failed to converge to the correct parameters values. Fig. 7.5 shows an example of two parameter search using Nelder-Mead Simplex search. We can see that Nelder-Mead algorithm soon stuck in a local minimum and was unable to climb out for the rest of the iterations. We suspect the reason Nelder-Mead Simplex search is less robust in nonconvex optimization is because the simplex "adapts itself to the local landscape", as expressed by the authors of the algorithm (Nelder and Mead, 1965), whereas the directions of Generalized Pattern Search are independent of the landscape. The landscape adaptive property of Nelder-Mead is useful in improving the solution quickly in just a few iterations (Lagarias et al., 1998), but this property

restricts the search directions of the algorithm when the current guess is in a local minimum. Thus, we concluded that Generalized Pattern Search is better suited for the nonconvex problem we have while searching for more than one parameter.

7.2 Parameter Estimation With Noise

In the previous chapter we talked about how noise can impact the performance of parameter estimation. We tested our parameter estimation method on various noise levels, and concluded our method worked best when signal-to-noise ratio is above 40. Here we will take a deeper look into the impact of noise on the parameter estimation.

7.2.1 Fracture Length Estimate

The results of estimating fracture length from noisy data (signal-to-noise ratio of 50) are shown in Fig. 7.6 and Fig. 7.7. We see both Generalized Pattern Search and Nelder-Mead Simplex algorithm converged to the correct solution, while taking a similar number of total function evaluations as the cases with perfectly measured data. Again, Nelder-Mead Simplex optimization converged to the correct solution faster than Generalized Pattern Search optimization.

In our study, Nelder-Mead Simplex optimization had better performance than Generalized Pattern Search optimization in one-dimensional search. Nelder-Mead Simplex optimization was able not only to converge to the correct solution faster than Generalized Pattern Search, but also was able to withstand stronger noise than Generalized Pattern Search as shown in Fig. 6.5.

7.2.2 Fracture Length And Fracture Density Estimate

We decided not to investigate further on optimization using Nelder-Mead Simplex method because the method failed to converge to the correct estimate of fracture length and fracture density when the data was perfectly measured. In addition, we have shown from sensitivity analysis in Fig. 6.8 that Nelder-Mead could not make the correct estimate when searching for two parameters at any noise level. On the other

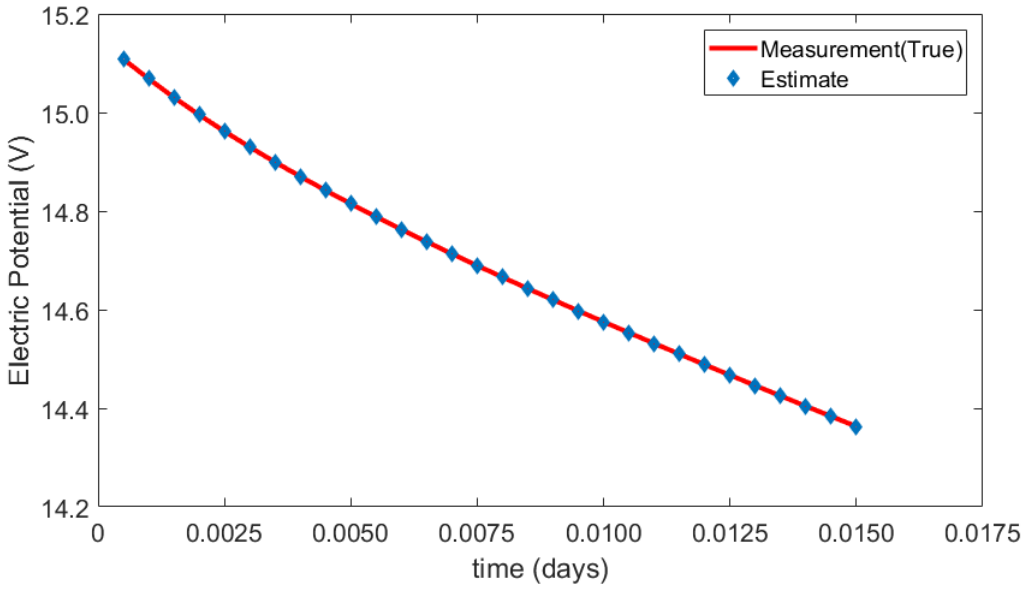

(a) Estimate of measurement data

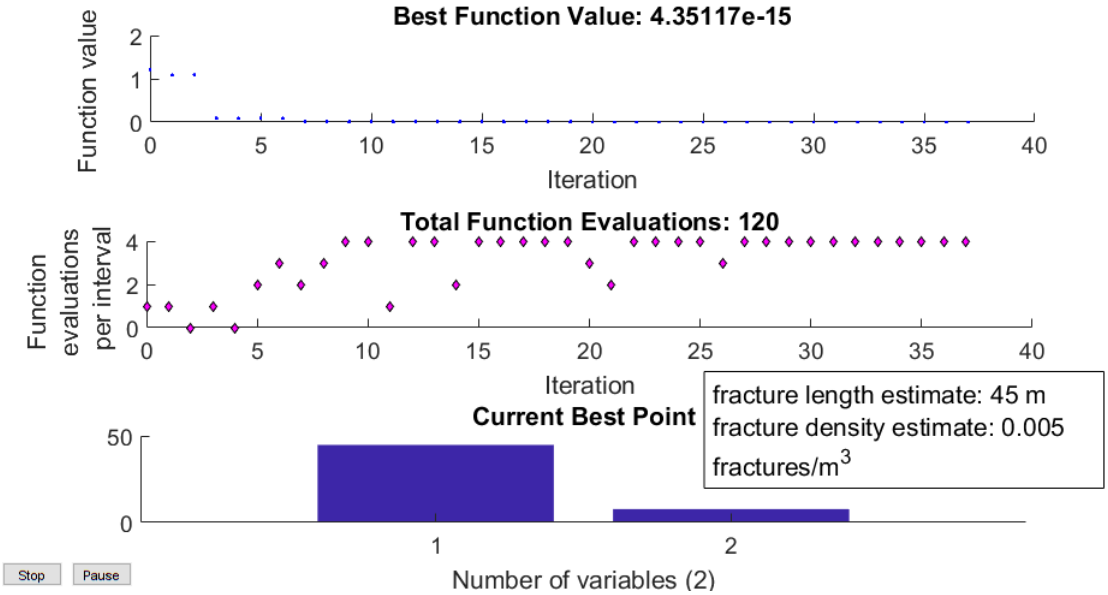

(b) Optimization information

Figure 7.4: Fracture length and fracture density estimate by applying Generalized Pattern Search on perfectly measured data.

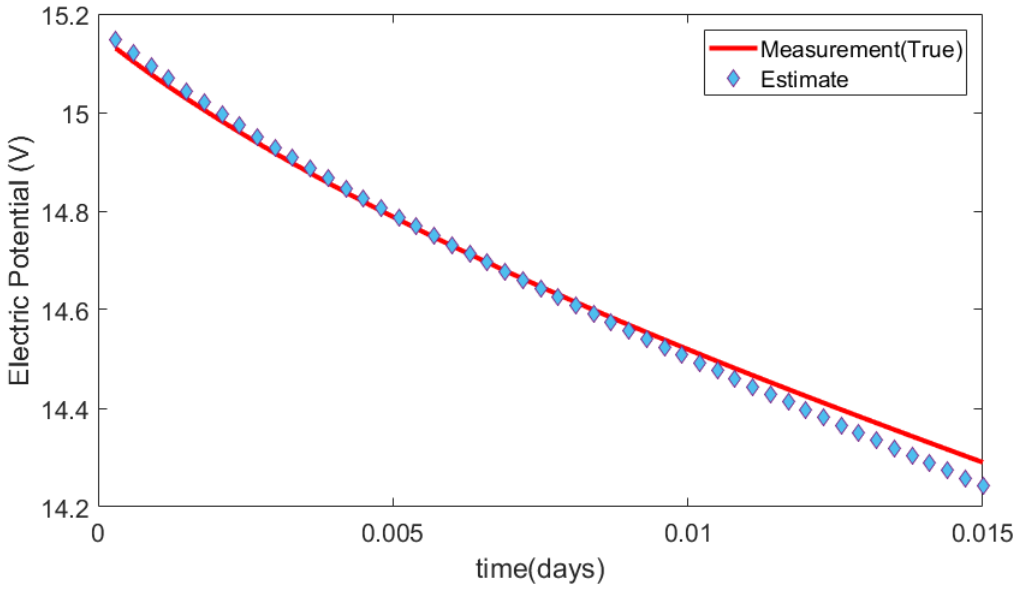

(a) Estimate of measurement data

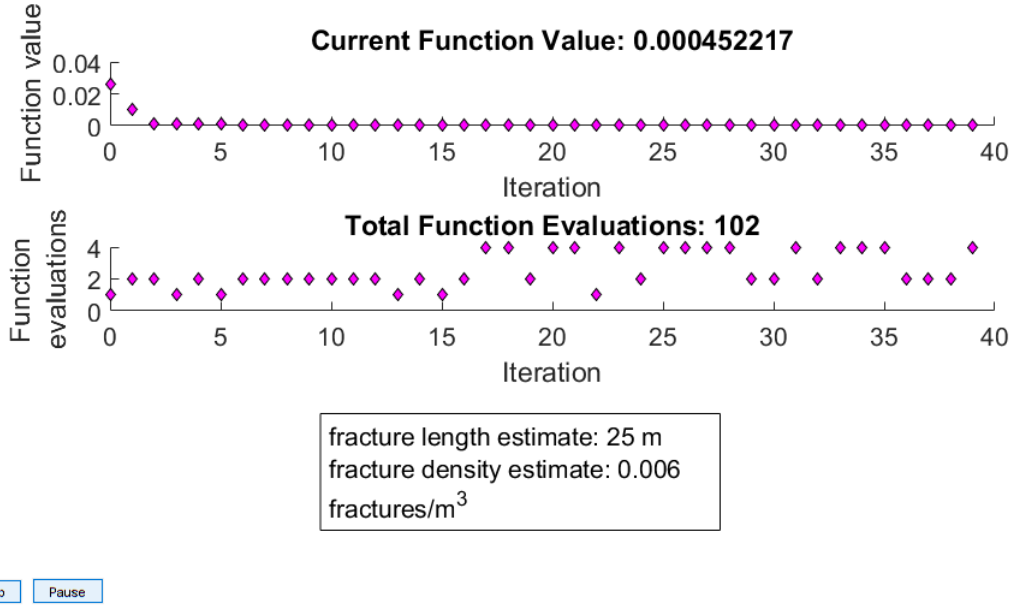

(b) Optimization information

Figure 7.5: Fracture length and fracture density estimate by applying Nelder-Mead on perfectly measured data.

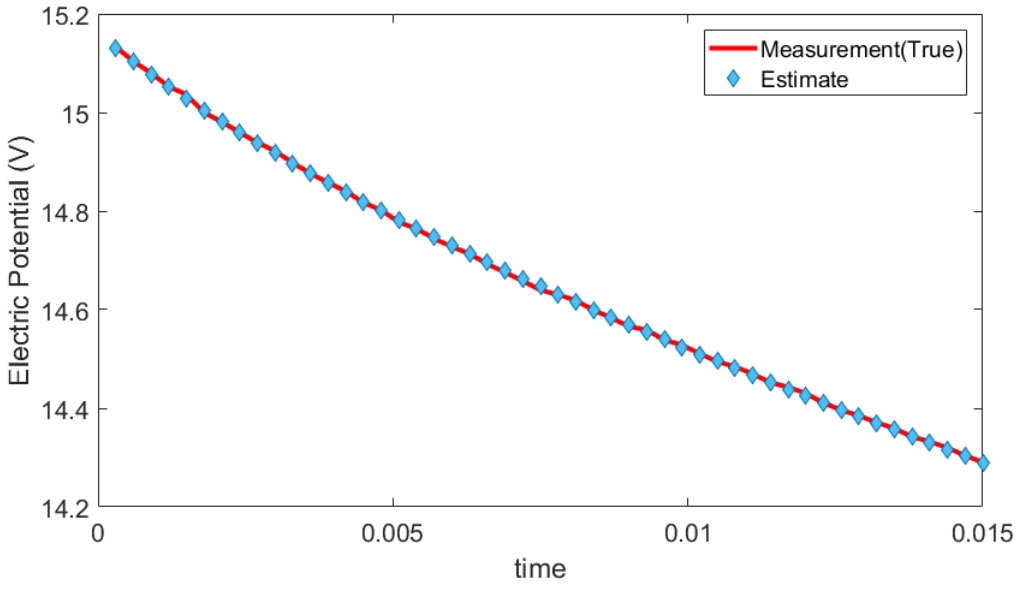

(a) Estimate of measurement data

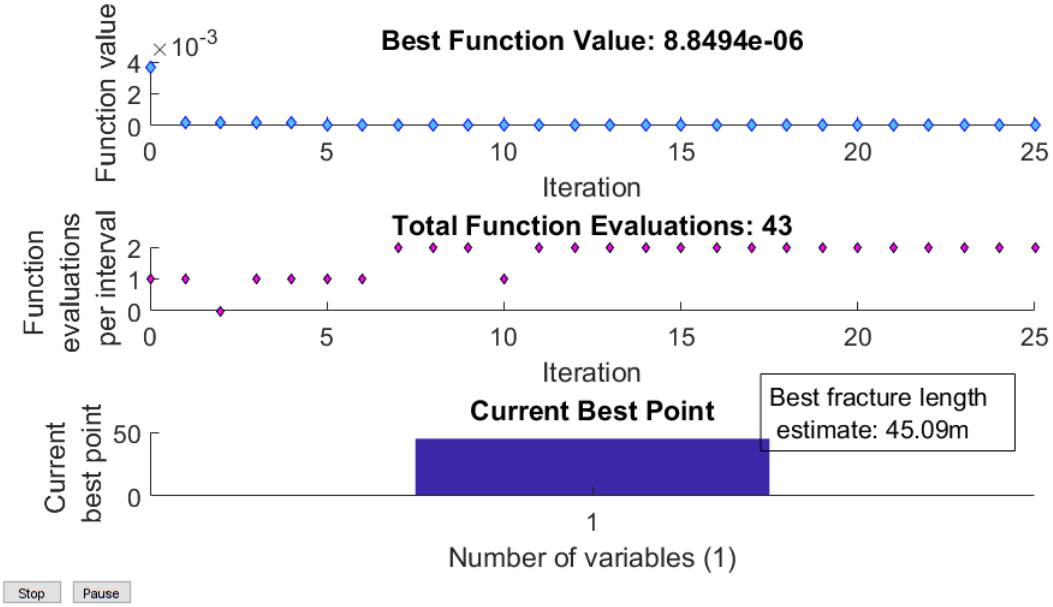

(b) Optimization information

Figure 7.6: Fracture length estimate by applying Generalized Pattern Search on noisy data with signal to ratio of 50.

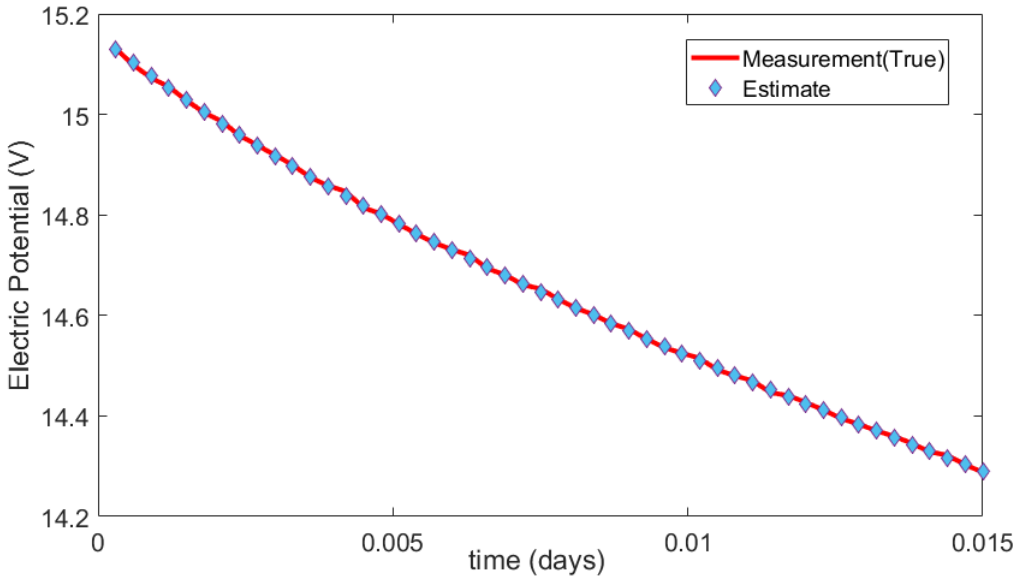

(a) Estimate of measurement data

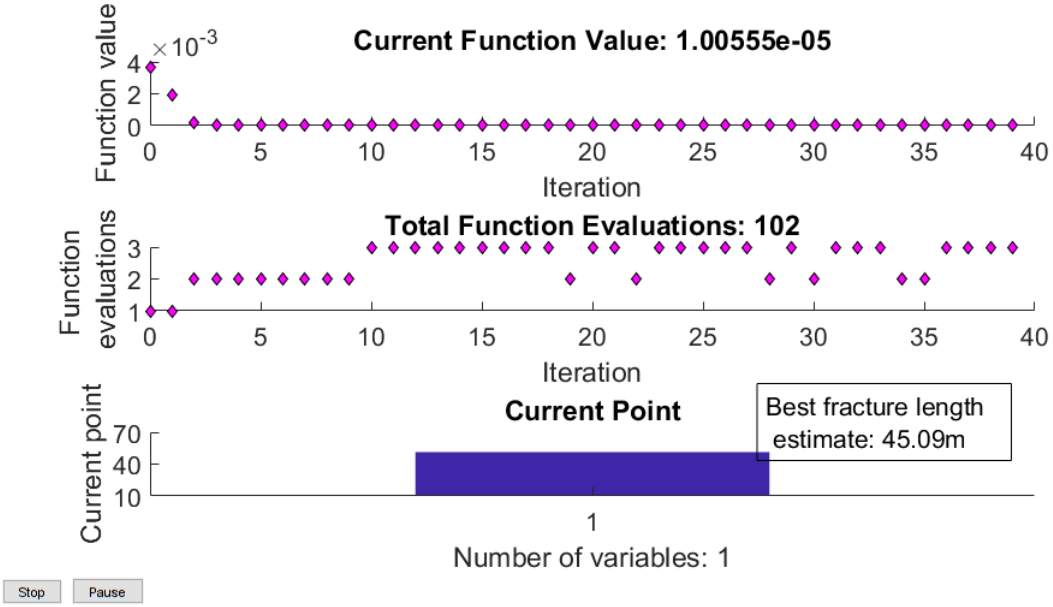

(b) Optimization information

Figure 7.7: Fracture length estimate by applying Nelder-Mead on noisy data with signal to ratio of 50.

hand, Generalized Pattern Search performed well in two parameter search scenarios. Fig. 7.8 shows an example of two parameter search using Generalized Pattern Search on noisy data.

7.2.3 Estimate Uncertainty

To evaluate the uncertainty of parameter estimates, we generated 30 different noise realizations at signal-to noise-ratio of 50. We took random guesses of fracture length and fracture density in each parameter search scenario and used Generalized Pattern Search to find the best estimates of parameters. Fig. 7.9 shows the 30 different electric potential data. Fig. 7.10 and Fig. 7.11 show the fracture length and fracture density estimate results. We can see our purposed search method is quite robust in estimating fracture length and density at signal-to-noise ratio of 50. The fracture length estimates are within 1 *meter* of the correct fracture length, and the relative errors of fracture length estimate are within 2%. Fracture density estimates are more uncertain than fracture length estimates, but the relative errors of fracture density estimate are still within 10%.

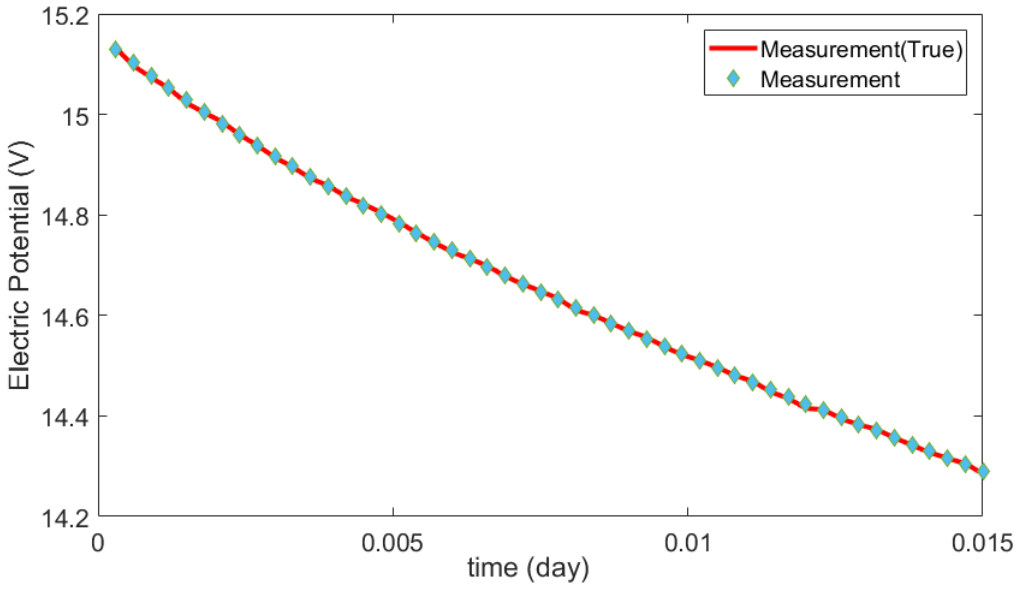

(a) Estimate of measurement data

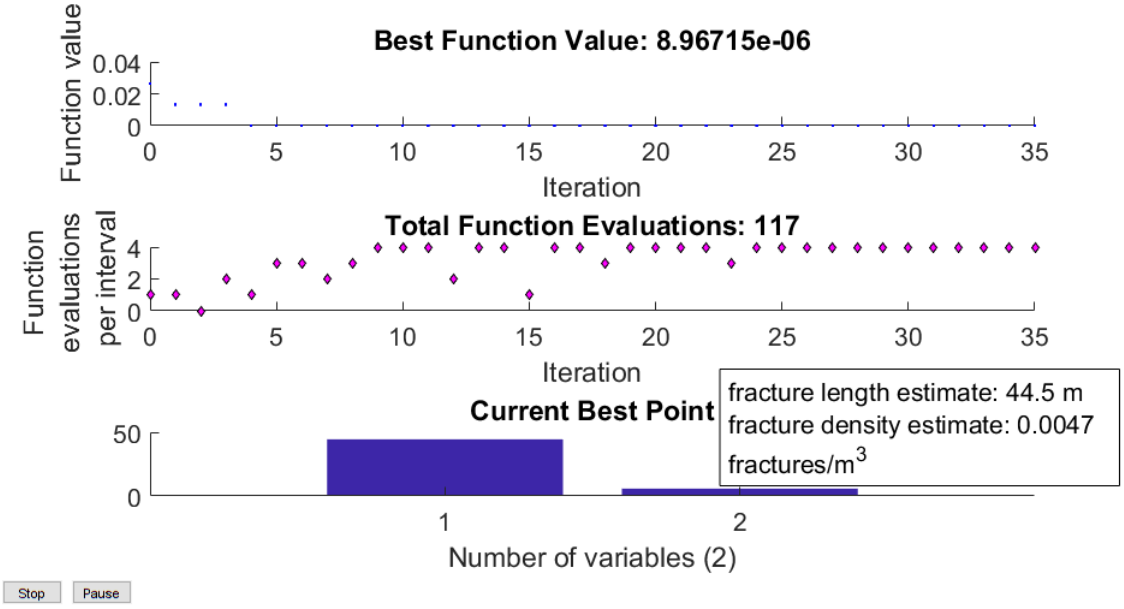

(b) Optimization information

Figure 7.8: Fracture length and fracture density estimate by applying Generalized Pattern Search on noisy data with signal to ratio of 50.

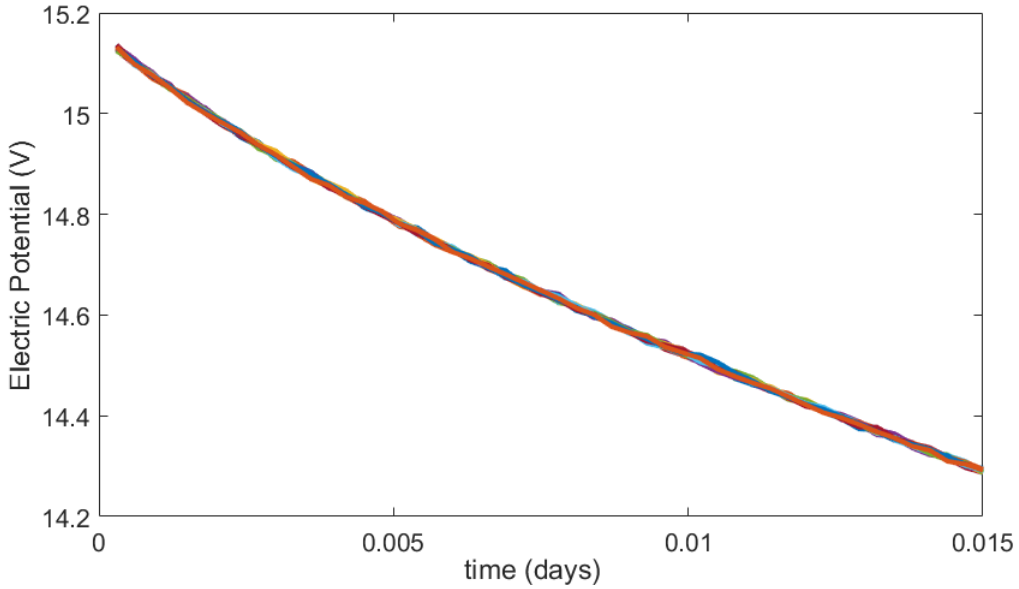

Figure 7.9: 30 noise realizations

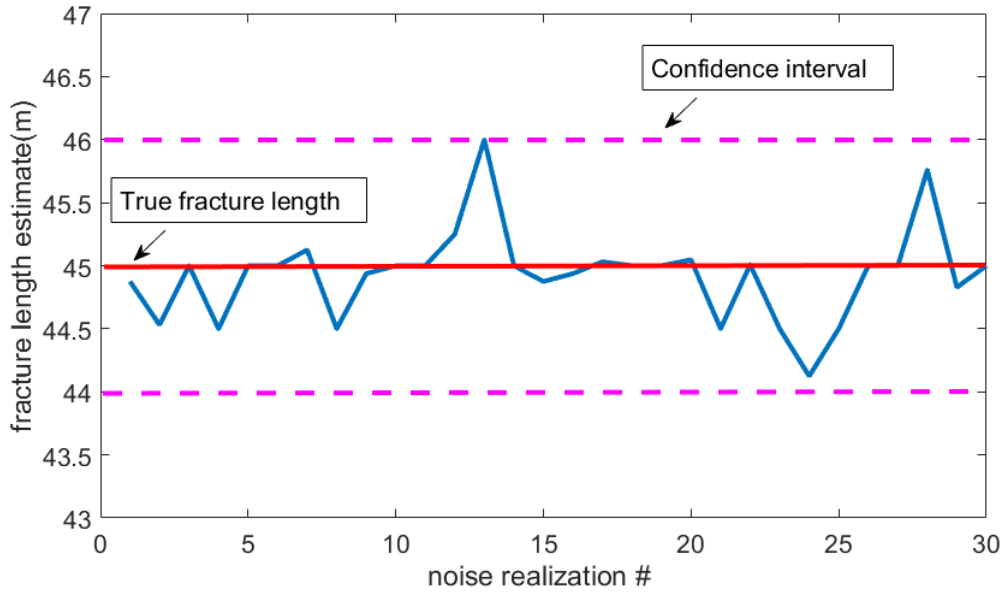

(a) Fracture length estimate

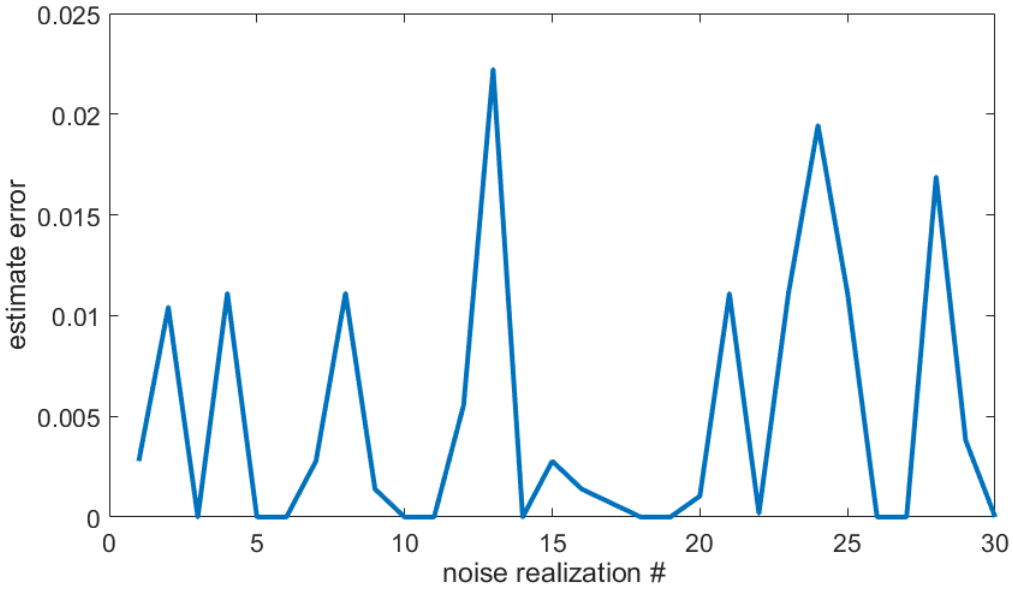

(b) Fracture length estimate error

Figure 7.10: Uncertainty of fracture length estimate at signal to noise ratio 50

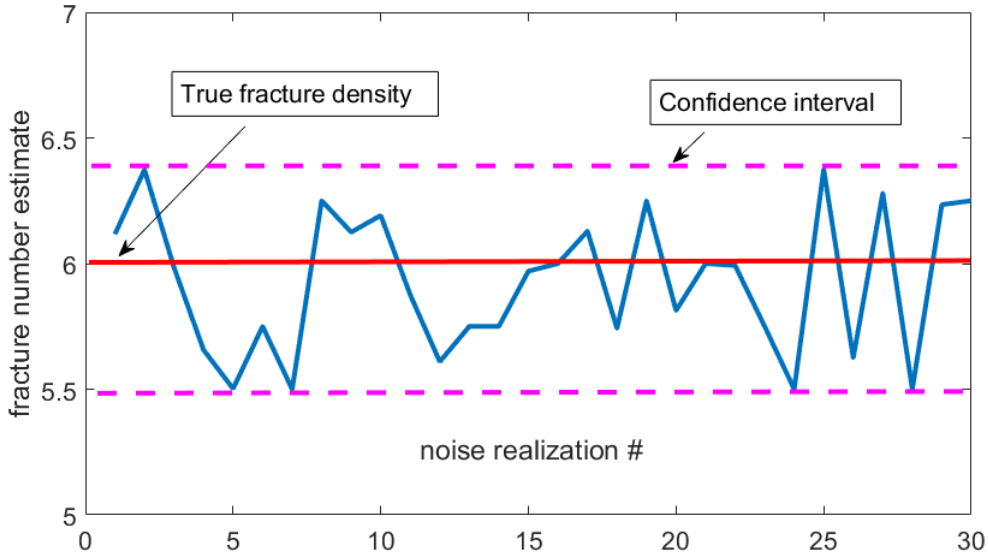

(a) Fracture density estimate

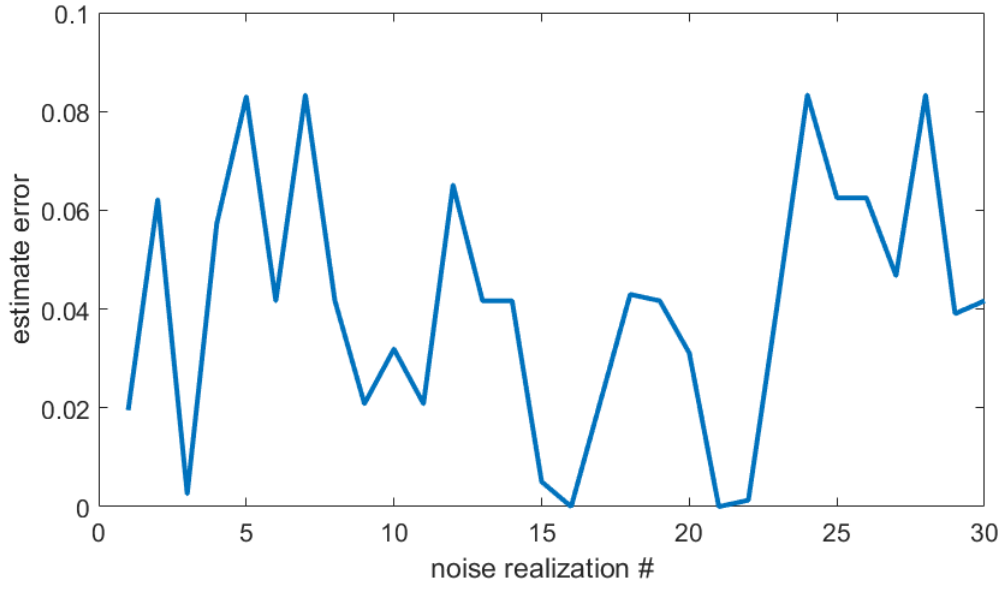

(b) Fracture density estimate error

Figure 7.11: Uncertainty of fracture density estimate at signal to noise ratio 50

Chapter 8

Concluding Remarks

8.1 Conclusion

In this study we built on the electrical resistivity data analysis framework and theoretical ground introduced by Wang (Wang, 1999) and Magnusdottir (Magnusdottir, 2013). We purposed a new electrical resistivity tool that can be used to record electric potential signal for horizontal wells in unconventional reservoirs, and integrated this tool into our simulation framework. We built a fractured model using Discrete Fracture Modeling and generated time-lapse electric potential signals by running electric simulation in parallel with flow simulation. The electric potential signal fully captured the dynamic fluid saturation distribution in rock formation during water injection process, and allowed our parameter estimation algorithm to estimate fracture length and fracture density. In our study we experimented with using Generalized Pattern Search and Nelder-Mead Simplex search as the nonlinear optimizer of our parameter estimation framework. While both Generalized Pattern Search and Nelder-Mead Simplex search estimated the correct fracture length successfully in one parameter search cases, only Generalized Pattern Search estimated the correct fracture length and fracture density successfully in two parameter search cases. We therefore performed additional analysis using Generalized Pattern Search as the nonlinear optimizer to ensure convergence. However, Nelder-Mead Simplex search was proven to have faster convergence and was more robust against noise in one parameter searches.

After we estimated fracture length and fracture density successfully using our purposed framework, we explored the capacity of our method by performing sensitivity analysis on electrode locations, injection fluid electrical conductivities, and noise levels. Through the sensitivity analysis we determined the best locations to place the electrodes, and concluded the purposed framework was robust in analyzing noisy data when the signal-to-noise ratio of the data was above 40.

8.2 Future Work

In our work we made strong assumptions about the pattern of fractures in our model, such that all the fractures were homogeneous and the spacings between fractures were equal. An additional step would be to solve potential differences for more realistic fracture patterns. The forward model could be parameterized by more fracture properties including fracture orientation, fracture permeability, fracture spacing, etc. The optimization scheme of the current framework should be reexamined to ensure convergence when the search dimensions are expanded to higher dimensional space. Genetic algorithm, mesh adaptive direct search (MADS), and particle swarm optimization maybe suitable candidates for higher dimensional searches.

We constructed our reservoir model in 2.5-dimensional and scaled down the reservoir size because of computation power constraint. Further improvement on the current model should include constructing the model in three-dimensional and increasing the scale of the model. Geomechanical fracture modeling should also be considered to capture more fracture characteristics.

The Ketzin pilot project (Schmidt-Hattenberger et al., 2017) and Cranfield CO_2 monitoring project (Carrigan et al., 2013) have shown that permanent downhole resistivity array can be used to monitor long term changes in subsurface fluid distribution. An interesting extension to our current study would be to investigate long term electric potential behavior of hydraulic fractured reservoirs in the production stage.

Nomenclature

α	Nelder-Mead reflection parameter
β	Nelder-Mead contraction parameter
δ	Dirac Delta function
γ	Nelder-Mead expansion parameter
μ	Magnitude of current density
ϕ	Porosity
ρ	Nelder-Mead shrinkin parameter
σ	Electrical conductivity
τ	Generalized Pattern Search optimization constant
$AD-GPRS$	Automatic-Differentiation General Purpose Research Simulator
c	Concentration
D	Generalized Pattern Search direction set
E	Electric field
G	Green's function
GPS	Generalized Pattern Search
J	Current density

$MADS$ Mesh adaptive direct search

MSE Mean squared error

q Current

T Temperature

V Voltage

Bibliography

Adachi, J. I. and Peirce, A. P. (2010). Analysis of the classical pseudo-3D model for hydraulic fracture with equilibrium height growth across stress barriers. *International Journal of Rock Mechanics and Mining Sciences*, 47(4):625–639.

Archie, G. (1942). The Electrical Resistivity Log as an Aid in Determining Some Reservoir Characteristics. *Transactions of the AIME*, 146(01):54–62.

Audet, C., Custódio, A. L., and Dennis, J. E. (2008). Erratum: Mesh Adaptive Direct Search Algorithms for Constrained Optimization. *SIAM Journal on Optimization*, 18(4):1501–1503.

Bennett, L., Calvez, J., Sarver, D. R. R., Tanner, K., Birk, W., Waters, G., Drew, J., Michaud, G., Primiero, P., Eisner, L., et al. (2005). The source for hydraulic fracture characterization. *Oilfield Review*, 17(4):42–57.

Binley, A. and Kemna, A. (2005). DC Resistivity and Induced Polarization Methods. *Hydrogeophysics*, pages 129–156.

Carrigan, C. R., Yang, X., LaBrecque, D. J., Larsen, D., Freeman, D., Ramirez, A. L., Daily, W., Aines, R., Newmark, R., Friedmann, J., and Hovorka, S. (2013). Electrical resistance tomographic monitoring of CO_2 movement in deep geologic reservoirs. *International Journal of Greenhouse Gas Control*, 18:401–408.

Dey A. and Morrison H.F. (1977). Resistivity Modeling for Arbitrarily Shaped Two-Dimensional Structures. *Geophysical Prospecting*, pages 106 – 136.

Geuzaine, C. and Remacle, J.-F. (2009). Gmsh: a three-dimensional finite element mesh generator with built-in pre-and post-processing facilities. *International Journal for Numerical Methods in Engineering 79(11)*, 0:1309–1331.

Glover, P. W. J. (2010). A generalized Archie's law for n phases. *Geophysics*, 75(6):E247–E265.

Greennberg, M. (1971). *Application of Green's Functions in Science and Engineering*. Prentice-Hall, Inc, Englewood Cliffs, New Jersey.

Hooke, R. and Jeeves, T. A. (1961). "Direct Search" Solution of Numerical and Statistical Problems. *Journal of the ACM (JACM)*, 8(2):212–229.

Horne, R. N. (1995). *Modern Well Test Analysis, A Computer-Aided Approach*. Petroway, Inc, Palo Alto, California, second edition.

Karimi-Fard, M. and Firoozabadi, A. (2001). Numerical Simulation of Water Injection in 2D Fractured Media Using Discrete-Fracture Model. *Proceedings of SPE Annual Technical Conference and Exhibition*.

Lagarias, J. C., Reeds, J. A., Wright, M. H., and Wright, P. E. (1998). Convergence Properties of the Nelder–Mead Simplex Method in Low Dimensions. *SIAM Journal on Optimization*, 9(1):112–147.

Magnusdottir, L. (2013). *Fracture Characterization in Geothermal Reservoirs Using Time-Lapse Electric Potential Data*. PhD thesis, Stanford University.

Magnusdottir, L. and Horne, R. N. (2015). Inversion of Time-Lapse Electric Potential Data Reservoirs. *Mathematical Geosciences*, 47(1):85–104.

Nelder, J. A. and Mead, R. (1965). A Simplex Method for Function Minimization. *The Computer Journal*, 7(4):308–313.

Rin, R., Tomin, P., Garipov, T., Voskov, D., and Tchelepi, H. (2017). General Implicit Coupling Framework for Multi-Physics Problems. *SPE Reservoir Simulation Conference*, (February).

Rios, L. M. and Sahinidis, N. V. (2013). Derivative-free optimization: A review of algorithms and comparison of software implementations. *Journal of Global Optimization*, 56(3):1247–1293.

Schmidt-Hattenberger, C., Bergmann, P., Kießling, D., Krüger, K., Rücker, C., and Schütt, H. (2011). Application of a Vertical Electrical Resistivity Array (VERA) for monitoring CO_2 migration at the Ketzin site: First performance evaluation. *Energy Procedia*, 4:3363–3370.

Schmidt-Hattenberger, C., Bergmann, P., Labitzke, T., Pommerencke, J., Rippe, D., Wagner, F., and Wiese, B. (2017). Monitoring the Complete Life-cycle of a CO_2 Storage Reservoir - Demonstration of Applicability of Geoelectrical Imaging. *Energy Procedia*, 114(November 2016):3948–3955.

Torczon, V. (1997). On the Convergence of Pattern Search Algorithms. *SIAM Journal on Optimization*, 7(1):1–25.

Ucok, H., Ershagi, I., and Olhoeft, G. R. (1980). Electrical Resistivity of Geothermal Brines. *Journal of Petroleum Technology*, 32(April):717–727.

Wang, P. (1999). Integrating Resistivity Data Into Parameter Estimation Problem. Master's thesis, Stanford University.

Wang, Z. and Bovik, A. C. (2009). Mean Squared Error: Love It or Leave It? A new look at signal fidelity measures. *IEEE Signal Processing Magazine*, 26(1):98–117.

Wright, C., Davis, E., Weijers, L., Golich, G., Ward, J., Demetrius, S., and Minner, W. (1998). Downhole Tiltmeter Fracture Mapping: A New Tool for Directly Measuring Hydraulic Fracture Dimensions. In *Proceedings of SPE Annual Technical Conference and Exhibition*.